bioRxiv preprint doi: https://doi.org/10.1101/805986; this version posted October 16, 2019. The copyright holder for this preprint (which was not certified by peer review) is the author/funder. All rights reserved. No reuse allowed without permission.

Specific decreasing of Na^+ channel expression on the lateral membrane of cardiomyocytes causes fatal arrhythmias in Brugada syndrome

Running title: *Tsumoto et al.; Na^+ Channel Expression and Arrhythmogenesis*

Authors: Kunichika Tsumoto[1,4]; Takashi Ashihara[2]; Narumi Naito[3]; Takao Shimamoto[3]; Akira Amano[3]; Yasutaka Kurata[1]; Yoshihisa Kurachi[4,5]

Affiliations:

[1]Department of Physiology, Kanazawa Medical University, Uchinada, Japan.

[2]Department of Medical Informatics and Biomedical Engineering, Shiga University of Medical Science, Otsu, Japan.

[3]Department of Bioinformatics, College of Life Sciences, Ritsumeikan University Kusatsu, Japan.

[4]Department of Pharmacology, Graduate school of Medicine, Osaka University, Suita, Japan.

[5]Global Center for Medical Engineering and Informatics, Osaka University, Suita, Japan.

Address for Correspondences:

Kunichika Tsumoto, PhD

Department of Physiology, Kanazawa Medical University, 1-1 Daigaku, Uchinada 920-0293, Japan. Phone: +81-76-286-2211, Fax: +81-76-286-8010. Email: tsumoto@kanazawa-med.ac.jp (K. Tsumoto) ORCID: 0000-0001-7457-3125

Non-standard Abbreviations and Acronyms: LM: lateral membrane of cardiomyocytes; JM: junctional membrane of cardiomyocytes; pre-JM: pre-junctional membrane of cardiomyocytes; post-JM: post-junctional membrane of cardiomyocyte; $I_{Na,LM}$: I_{Na} across the LM; $I_{Na,pre\text{-}JM}$: I_{Na} across the pre-JM; $I_{Na,post\text{-}JM}$: I_{Na} across the post-JM; $V_{m,pre\text{-}JM}$: membrane potential of the pre-JM; $V_{m,post\text{-}JM}$: membrane potential of the post-JM

bioRxiv preprint doi: https://doi.org/10.1101/805986; this version posted October 16, 2019. The copyright holder for this preprint (which was not certified by peer review) is the author/funder. All rights reserved. No reuse allowed without permission.

ABSTRACT

One phenotypic feature of Brugada syndrome (BrS) is slowed conduction due to the reduction (loss-of-function) of Na^+ channels. In contrast, recent clinical observations in BrS patients highlighted the poor correlation between the phenotype (typical ECG change or lethal arrhythmia) and the genotype (*SCN5A* mutation). Inspired by our previous theoretical study which showed that reduced Na^+ channels in the lateral membrane (LM) of ventricular myocytes caused the slowing of conduction under myocardial ischemia, we hypothesized that a loss-of-function of Na^+ channels caused by the decreases in Na^+ channel expression within myocytes leads to phase-2 reentry (P2R), the major triggering mechanism of lethal arrhythmias in BrS. We constructed an *in silico* human ventricular myocardial strand and ring models, and investigated the relationship between the subcellular Na^+ channel distribution and P2R. Reducing Na^+ channel expression in the LM of each myocyte caused not only the notch-and-dome but also loss-of-dome type action potentials and slowed conduction, both of which are typically observed in BrS patients. Furthermore, we showed that both the reduction in Na^+ channels on the LM of each myocyte and tissue-level heterogeneity of Na^+ channel expression were essential for P2R as well as P2R-mediated reentrant excitation. Our data suggest that the alteration in subcellular Na^+ channel distribution together with a tissue-level heterogeneity of Na^+ channels can cause arrhythmogenesis in BrS.

Key words: Brugada syndrome, phase-2 reentry, sodium channel, conduction delay, computer simulations

bioRxiv preprint doi: https://doi.org/10.1101/805986; this version posted October 16, 2019. The copyright holder for this preprint (which was not certified by peer review) is the author/funder. All rights reserved. No reuse allowed without permission.

Introduction

Cardiac Na^+ channel current (I_{Na}) that controls the excitability of cardiomyocytes mainly contributes to the action potential (AP) initiation and its propagation. Na^+ channel dysfunction in congenital or acquired heart diseases leads to decreases in the I_{Na}, which has been associated with slowed or blocked conduction, resulting in a potentially proarrhythmic substrate. Genetic abnormalities causing Na^+ channel dysfunction have been linked to many arrhythmogenic diseases (*1*), including sick sinus syndrome, progressive cardiac conduction disorders, and Brugada syndrome (BrS). In contrast, a previously published study suggested that variants of *SCN5A*, which is one of the important disease genes for BrS (*2*), were not necessarily associated with the BrS phenotype (*3*). The loss-of-function mutations in *SCN5A* are not a determinant factor of BrS.

BrS is characterized by the ECGs with both a right bundle-branch block pattern and ST-segment elevation in the right precordial leads (V_1-V_3) and by the higher incidence of sudden cardiac death due to ventricular tachycardia/fibrillation (VT/VF) (*4*, *5*). It is commonly believed that VT/VF is elicited by the closely coupled premature ventricular contractions via the phase-2 reentry (P2R) mechanism (*6*). This mechanism is caused by an electrotonic current flowing from the region where AP exhibits notch-and-dome morphology to the region where AP shows loss of the phase-2 dome. Although at first, it has been predicted that a global difference in AP duration (APD) causing a transmural voltage gradient in the right ventricle (RV) is a cause of P2R development (*4*), several experimental studies using an optical mapping system showed that the epicardial local APD difference was involved in the occurrence of P2R (*7*, *8*). Thus, the P2R mechanism in BrS is still controversial.

bioRxiv preprint doi: https://doi.org/10.1101/805986; this version posted October 16, 2019. The copyright holder for this preprint (which was not certified by peer review) is the author/funder. All rights reserved. No reuse allowed without permission.

Previous experimental studies (*9*, *10*) have produced knock-in mice lacking the SIV (Serine-Isoleucine-Valine) domain (ΔSIV) of the $Na_V1.5$ PDZ domain–binding motif that interacts with PDZ proteins (syntrophin and SAP97). Experiments on these mice showed that both Na^+ channel expression and I_{Na} on the lateral membrane (LM), but not on the intercalated discs (IDs), of cardiomyocytes were decreased. This led to slowed conduction at the tissue level. Notably, Shy et al. (*10*) identified a missense mutation within the SIV motif (p.V2016M) from a patient with BrS, suggesting that the local alteration in subcellular Na^+ channel expression as observed in the ΔSIV mice might be involved in BrS. In a previous theoretical study (*11*), we showed that a subcellular alterations in Na^+ channel expression induced by myocardial ischemia, specifically reduced number of Na^+ channels in the LM of cardiomyocytes, was strongly associated with both the decrease in local I_{Na} and slowed conduction. Furthermore, the local decreasing of I_{Na} in cardiomyocytes evoked P2R. Therefore, we hypothesized that a local alteration in subcellular Na^+ channel expression may lead to the development of P2R and VT/VF in BrS. To rigorously examine this hypothesis, we require an analyzing system in which Na^+ channel expression within each myocyte can be selectively controlled. We, therefore, developed *in silico* human ventricular myocardial strand and ring models reflecting the recent experimental data (*10*) on subcellular Na^+ channel expression changes observed in the ΔSIV mice. Then, we performed simulations of AP propagation in the *in silico* models and investigated the relationship between the subcellular alterations in Na^+ channel expression and the occurrence of P2R leading to reentrant arrhythmia onsets in BrS.

bioRxiv preprint doi: https://doi.org/10.1101/805986; this version posted October 16, 2019. The copyright holder for this preprint (which was not certified by peer review) is the author/funder. All rights reserved. No reuse allowed without permission.

Methods

Myocardial strand and ring models and subcellular Na^+ channel distribution

To perform computer simulations examining effects of alterations in subcellular Na^+ channel distribution on AP propagation behaviors, we used myocardial strand (Fig. 1A and fig. S1) and ring (Fig. 1D) models comprised of cylindrical human ventricular myocytes, each 150 μm in length and 20 μm in diameter (*12*). As shown in Fig. 1B, adjacent myocytes were electrically coupled with both gap junctions and an electric field mechanism (ephaptic coupling) (*13*, *14*), the latter of which is an interference effect caused at intercellular cleft space; electrical communication between myocytes through the electric field mechanism is mediated by large negative changes in the extracellular potential elicited within the narrow intercellular cleft space facing the IDs.

As in our previous study (*11*), to achieve the inhomogeneous Na^+ channel distribution within a myocyte found in humans and other mammals (*15*), the whole cell membrane of each myocyte was divided into three segments (Fig. 1C), one segment for the LM and the other two segments for the junctional membranes (JMs), namely the IDs. Allocating Na^+ channel conductances to each membrane segment and changing those individually, we altered the subcellular expression of Na^+ channels. The electrophysiological property of each membrane segment was represented by the O'Hara-Rudy dynamic (ORd) model (*16*, *17*), which is the most sophisticated human ventricular AP model to date that extensively validated against experimental data from more than 100 non-diseased human hearts. For better correspondence with the experimental conduction velocity of human RV epicardium (*18*), the formula of fast I_{Na} in the ORd model was replaced with that of the ten Tusscher-Panfilov (TP) model (*19*). We set the control conductance of fast I_{Na} to 11 nS/pF for the LM ($G_{NaF,LM}$) and 44

bioRxiv preprint doi: https://doi.org/10.1101/805986; this version posted October 16, 2019. The copyright holder for this preprint (which was not certified by peer review) is the author/funder. All rights reserved. No reuse allowed without permission.

nS/pF for the JMs ($G_{NaF,JM}$) so that I_{Na} amplitude obtained from the simulation matched the one recorded experimentally for basal condition (*10*); the conductance of late I_{Na} was also set to 0.0045 nS/pF for the LM ($G_{NaL,LM}$) and 0.018 nS/pF for the JMs ($G_{NaL,JM}$) as the control condition. Throughout the article, we express the fast and late Na^+ channel conductances of the JM and LM as percentages of the $G_{NaF,JM}$ ($G_{NaL,JM}$) and $G_{NaF,LM}$ ($G_{NaL,LM}$), i.e., $\%g_{Na,JM}$ and $\%g_{Na,LM}$, respectively. Specific parameters in the myocardial strand and ring models consisting of the ORd model can be found in the supplemental table S1.

Simulations

Numerical calculations were performed as described previously (*11*) and details were provided in Supplementary Materials. Pacing stimuli at threefold diastolic threshold with a basic cycle length of 1 s were applied to a myocyte located at the end of the myocardial strand (the 300th myocyte in the myocardial ring) and repeated 30 times to minimize transient responses in each simulation. The membrane potential was calculated using the forward Euler method with a 1 μs time step to compensate for the reduced size of the discretized space and for the acute change in the membrane potential at the IDs due to the electric field mechanism.

To test whether the sympathetic activity inhibits the P2R development, we additionally performed simulations of AP propagation using the myocardial strand model under the condition of β-adrenergic stimulation (β-AS) mimicking sympathetic activation. Modifications of parameters for simulating the condition of β-AS (*20, 21*) were listed in the supplemental table S2.

bioRxiv preprint doi: https://doi.org/10.1101/805986; this version posted October 16, 2019. The copyright holder for this preprint (which was not certified by peer review) is the author/funder. All rights reserved. No reuse allowed without permission.

Results

Reducing Na^+ channel conductance in the LM causes AP morphological changes

First, we examined effects of alterations in subcellular Na^+ channel expression on AP propagation by using a homogeneous myocardial strand model consisting of 300 cells. When the Na^+ channel conductance of the LM (%$g_{Na,LM}$) in each myocyte of the myocardial fiber was set to the control condition, the APs propagated through the myocardial strand (Fig. 2A*a*) and exhibited a typical human ventricular AP morphology (Figs. 2A*a* and 2B*a*, red line). To test how the selective decreasing of Na^+ channel expression on the LM of myocytes as demonstrated by Shy et al (*10*) affects AP propagation, the %$g_{Na,LM}$ in each myocyte of the myocardial fiber was reduced homogeneously. Reducing the %$g_{Na,LM}$ by 65% resulted in the decrease in the $I_{Na,LM}$ peak in the 150th cell by 57.9% (Fig. 2B*b*, cyan line) and slightly shortened the APD; APD at 90% repolarization (APD_{90}) was 235.2 ms in 35%$g_{Na,LM}$ versus 240.0 ms in 100%$g_{Na,LM}$ (Figs. 2A*b* and 2B*a*, and Tables 1 and 2). These results were similar to those experimentally determined by the previous study (*8*, see table S3**)**. Markedly reducing Na^+ channels from the LM of each myocyte (7%$g_{Na,LM}$) resulted in the $I_{Na,LM}$ decrease by 92.5% (Fig. 2B*b*, blue line), diminished AP phase-0 amplitude and produced a larger phase-1 dip in the AP. As a result, the peak of the phase-2 dome was markedly delayed (Figs. 2A*c* and 2B*a*, blue lines). APD_{90} that delayed the phase-2 dome peak was 15.8 ms longer than that of the control condition (100%$g_{Na,LM}$, see Table 2). Moreover, the loss of Na^+ channels in the LM of each myocyte (0%$g_{Na,LM}$) caused a further decrease in the AP phase-0 amplitude (Fig. 2B*a*, green line), resulting in the failure of the transient outward K^+ channel current (I_{to}) and L-type Ca^{2+} channel current (I_{CaL}) to activate normally (Figs. 2B*c* and 2B*d*, green lines). The transient

bioRxiv preprint doi: https://doi.org/10.1101/805986; this version posted October 16, 2019. The copyright holder for this preprint (which was not certified by peer review) is the author/funder. All rights reserved. No reuse allowed without permission.

activation of the rapid component of delayed rectifier K^+ channel current (I_{Kr}) and the Na^+-K^+ pump current (I_{NaK}), and subsequent activation of the inward rectifier K^+ channel current (I_{K1}), the late peak of which appeared earlier, allowed for earlier repolarization (Figs. 2B*e*, 2B*g* and 2B*h*). The slow component of delayed rectifier K^+ channel current (I_{Ks}) hardly contributed to the repolarization (Fig. 2B*f*, green line). This, in turn, led to AP propagation with a shortened APD (Fig. 2A*d*).

These alterations in subcellular Na^+ channel distribution also modified the conduction velocity (CV). The pre-JM current ($I_{m,pre\text{-}JM}$; figs. S2A and S2B, orange lines) is the difference between the post-JM current ($I_{m,post\text{-}JM}$; fig. S2B, purple lines) and the transmembrane current in the LM (see fig. S2C, gray lines), and is determined by G_i and $V_{i,LM} - V_{i,pre\text{-}JM}$, where $V_{i,LM}$ and $V_{i,pre\text{-}JM}$ are the intracellular potentials in the LM and pre-JM compartments, respectively (see figs. S2A and S2D). The decrease in $I_{Na,LM}$ (%$g_{Na,LM}$ from 100% to 0%) caused a decrease in the maximum upstroke velocity of $V_{i,LM}$ (compare gray lines in left to right panels of fig. S2D and see Table 2). The decrease in $V_{i,LM} - V_{i,pre\text{-}JM}$ also reduced $I_{m,pre\text{-}JM}$ (compare orange lines in left to right panels of fig. S2B), resulting in the decrease in maximum upstroke velocity of $V_{i,pre\text{-}JM}$, $\dot{V}^{max}_{i,pre-JM}$, (compare orange lines in left to right panels of fig. S2D). Thus, the decrease in $\dot{V}^{max}_{i,pre-JM}$ caused a decrease in the difference between the $V_{i,pre\text{-}JM}$ and the intracellular potential of the post-JM compartment ($V_{i,post\text{-}JM}$; purple lines in fig. S2D) in the neighbor myocyte. Subsequently, this led to both a marked decrease in the gap junctional current (I_g) defined by the equation $I_g = G_g \times \left(V^{150}_{i,pre-JM} - V^{151}_{i,post-JM}\right)$ for 150th myocyte (compare colored lines in left to right panels of fig. S2E) and a decrease in CV (see Table 1).

bioRxiv preprint doi: https://doi.org/10.1101/805986; this version posted October 16, 2019. The copyright holder for this preprint (which was not certified by peer review) is the author/funder. All rights reserved. No reuse allowed without permission.

Combination of the decreases in Na^+ channel expression on the LM in myocytes and the spatially-heterogeneous Na^+ channel distribution in tissue led to P2R development

To test our hypothesis that alterations in the subcellular Na^+ channel distribution lead to the development of P2R, we investigated the combined effects of both the regional I_{Na} decrease on the LM in myocytes and the spatial heterogeneity of Na^+ channels in the myocardial tissue on AP propagation. The spatial heterogeneity of Na^+ channels in the myocardial strand was achieved by changing the $\%g_{Na,LM}$ in the proximal part of the myocardial strand (200 myocytes), while maintaining the $7\%g_{Na,LM}$ (0.77 nS/pF) in the distal part of the myocardial strand (100 myocytes). The AP conduction exhibited AP alternans (Fig. 3A*a*) when the $\%g_{Na,LM}$ of the proximal myocytes was set to 0.66 nS/pF ($6\%g_{Na,LM}$), as the slight spatial heterogeneity of Na^+ channels in the myocardial strand. The spatial heterogeneity augmentation by further reducing the $\%g_{Na,LM}$ in the proximal myocytes led to proarrhythmic changes such that the AP dome was lost in the proximal myocytes and P2R followed (Fig. 3A*b*).

To understand relationships among Na^+ channel distributions within myocytes, spatial heterogeneous Na^+ channel distribution in tissue, and development of P2R, we systematically performed simulations of AP propagations while changing the subcellular Na^+ channel distribution in the proximal and distal parts of the myocardial fiber every $1\%g_{Na,LM}$. Fig. 3B shows a phase diagram constructed by mapping the AP propagation patterns obtained from each simulation on the parameter plane of the $\%g_{Na,LM}$ in proximal and distal myocytes. Open circles labeled as "*a*" and "*b*" in Fig. 3B correspond to Figs. 3A*a* and 3A*b*, respectively. We can see that the 2:1

bioRxiv preprint doi: https://doi.org/10.1101/805986; this version posted October 16, 2019. The copyright holder for this preprint (which was not certified by peer review) is the author/funder. All rights reserved. No reuse allowed without permission.

retrograde P2R as shown in Fig. 3A*b* occurred when the %$g_{Na,LM}$ in the proximal myocyte was reduced to < 5% regardless of the %$g_{Na,LM}$ in the distal myocytes (Fig. 3B, purple region), and that the region that P2R occurs was largely the left upper region of the diagonal line which represents conditions of spatially-homogeneous Na^+ channel distribution in myocardial strand. This implies that P2R occurs when a spatially-heterogeneous Na^+ channel distribution exists on the myocardial fiber. These results suggest that selective decrease in Na^+ channels on the LM of myocytes and the spatially-heterogeneous Na^+ channel expression on the myocardial tissue cooperatively facilitate the occurrence of P2R.

I_{CaL} plays an important role in the P2R development

Based on the results shown in Fig. 3, we focused on how AP morphology is affected by changes in the ion channel currents. Fig. 4 shows the AP profiles and main ion channel currents in several myocytes near the border between the proximal and distal parts of the myocardial fiber during the development of the 2:1 P2R shown in Fig. 3A*b*. The initial depolarization of the regional membrane potential (V_m) in the LM segment of each myocyte, i.e., that is equal to $V_{i,LM}$, within the proximal part of the myocardial strand (#140, 160 and 180 in Fig. 4B, asterisk) was formed by the local current flows consisting of I_g (Fig. 4C) and post-$I_{Na,JM}$ (Fig. 4D*a*). These current flows entered the myocyte through the post-JM. However, the local current was not able to depolarize the LM sufficiently (Fig. 4B, green line), and both I_{CaL} and I_{to} failed to activate (Fig. 4E*a*-*b*, green lines). Moreover, the relatively large transient I_{Kr} activation (Fig. 4E*c*, green line) and faster onset of the late peak of I_{K1} in the proximal myocyte (Fig. 4E*d*, dagger) accelerated the AP repolarization with the loss of AP dome (Figs. 4A and 4B).

bioRxiv preprint doi: https://doi.org/10.1101/805986; this version posted October 16, 2019. The copyright holder for this preprint (which was not certified by peer review) is the author/funder. All rights reserved. No reuse allowed without permission.

Subsequently, the difference in V_m at the border between proximal and distal parts was increased, and consequently this elicited the retrograde I_g (the inward currents in Fig. 4C) from the distal to the proximal part. Unlike the anterograde I_g elicited by the initial depolarization differences in neighbor myocytes within the proximal part, the retrograde I_g continued to flow for a relatively long time because the notch-and-dome type prolonged AP in distal myocytes caused a long-lasting potential difference from the proximal loss-of-dome abbreviated AP. Continuous depolarizing loads of the proximal myocytes by the long-lasting retrograde I_g allow the depolarization of the V_m that activates I_{CaL} of the LM in proximal myocytes, leading to re-excitation of the myocytes in the proximal part, i.e., retrograde P2R (Fig. 4A).

This theoretical model for the P2R mechanism can also be used to investigate the mechanism of P2R inhibition. We conducted an additional, identical simulation under a β-AS condition (*20*, *21*). The marked increase in I_{CaL} due to the β-AS effect kept the AP dome of each myocyte even under the smaller $\%g_{Na,LM}$ condition that caused loss-of-dome type abbreviated AP by the marked decrease in $I_{Na,LM}$ in the proximal part of the myocardial fiber without β-AS (see Fig. 5). This resulted in an increase in V_m amplitude and APD prolongation in the proximal and distal parts of the myofiber (compare Fig. 5B and Fig. 4B). Thus, β-AS that causes an increase in I_{CaL} is effective for preventing P2R.

The P2R triggered reentrant arrhythmias

Whether or not the P2R triggers reentrant arrhythmias was investigated using a myocardial ring model. In the myocardial ring with spatially-homogeneous Na^+ channel distribution (Fig. 6A), the AP exhibited bidirectional conduction from the

bioRxiv preprint doi: https://doi.org/10.1101/805986; this version posted October 16, 2019. The copyright holder for this preprint (which was not certified by peer review) is the author/funder. All rights reserved. No reuse allowed without permission.

stimulus site (300th myocyte), resulting in the collision of excitation wavefronts at the opposite side of the stimulus site (Fig. 6A*a*, asterisk). When the %$g_{Na,LM}$ from the LM of each myocyte in the myocardial ring was homogeneously reduced by 95%, the bidirectional conduction of shortened AP from the stimulus site was observed (Fig. 6A*b*); the bidirectional excitation wavefronts collided, causing a bidirectional P2R in the myocardial ring. However, each excitation wavefront originating from the bidirectional P2R collided and disappeared at around stimulus site (Fig. 6A*b*); no proarrhythmic changes were observed in the myocardial ring model with spatially-homogeneous Na^+ channel distribution even under the condition of the markedly decreased %$g_{Na,LM}$. However, in the same myocardial ring model but with the spatially-heterogeneous Na^+ channel distribution (Fig. 6B), AP conduction properties obviously changed (see Figs. 6B*a* and 6B*b*). With maintaining the %$g_{Na,LM}$ of 100 cells (cells #1-100; region A in Fig. 6B) at 5% (0.55 nS/pF), the %$g_{Na,LM}$ in each 500 cells (cells #101-600; region B in Fig. 6B) was uniformly reduced to 3% (0.33 nS/pF), producing the spatial heterogeneity of Na^+ channel distribution within the tissue. The bidirectional excitation wavefronts elicited at the stimulus site (cell #300) collided at the border between the regions A and B (Fig. 6B*a*, asterisk) and were subsequently followed by bidirectional P2R occurrence. However, the clockwise-rotating excitation wave of the P2R exhibited decremental conduction and block (Fig. 6B*a*, dagger); in contrast, the counterclockwise-rotating excitation wave continued to conduct in the myocardial ring, causing the P2R-mediated reentrant tachyarrhythmias. During 1-Hz pacing, the occurrence of reentrant arrhythmias was intermittent and irregular (see fig. S3A). The further augmentation of the spatial heterogeneity of Na^+ channel distribution in the

bioRxiv preprint doi: https://doi.org/10.1101/805986; this version posted October 16, 2019. The copyright holder for this preprint (which was not certified by peer review) is the author/funder. All rights reserved. No reuse allowed without permission.

tissue (5%$g_{Na,LM}$ in region A and 2%$g_{Na,LM}$ in region B on the myocardial ring) induced P2R-mediated persistent reentry (Figs. 6B*b* and S3B).

Discussion

Although it has so far believed that the loss-of-function mutation of Na^+ channels is one of the major causes of fatal arrhythmias in patients with BrS, the link between the loss-of-function of Na^+ channels and arrhythmogenesis was not clear. In the present study, we found that selective decreases in $I_{Na,LM}$ of each ventricular myocyte caused both morphological changes in AP and the conduction slowing that are typically observed in BrS patients (*22*, *23*). These findings suggest that both the BrS mechanisms, previously represented as repolarization and depolarization abnormalities (*24*), can at least in part be explained by this decrease in $I_{Na,LM}$. Furthermore, we showed that the marked decrease in $I_{Na,LM}$ together with an existence of the spatial heterogeneity at tissue-level in the Na^+ channel expression is essential for the P2R development, as well as the reentry initiation triggered by the P2R. To the best of our knowledge, this is the first report demonstrating mechanistic links between subcellular Na^+ channel expression changes mediated loss-of-function of Na^+ channels and P2R in BrS.

Decreasing $I_{Na,LM}$ causes the BrS notch and dome AP morphology

An alteration in the subcellular Na^+ channel expression with the marked reduction in Na^+ channels in the LM (%$g_{Na,LM}$ to 7%) resulted in the notch-and-dome AP morphology (Fig. 2A*c* and 2B*a*, blue line). Selectively reducing Na^+ channels from the LM largely reduced the AP phase-0 amplitude (Fig. 2B*a*, blue line). Because both I_{to}

bioRxiv preprint doi: https://doi.org/10.1101/805986; this version posted October 16, 2019. The copyright holder for this preprint (which was not certified by peer review) is the author/funder. All rights reserved. No reuse allowed without permission.

and I_{CaL} activate as V_m exceeds −30 mV (*16*), the underdeveloped AP phase-0 amplitude resulted in a marked decrease in I_{to} during AP phase-1 and the delay of I_{CaL} activation (Figs. 2B*c* and 2B*d*, blue lines). The decrease in I_{to} and delay in I_{CaL} activation led to a large phase-1 dip and the delay of the AP phase-2 dome peak, respectively. This morphology resembled that of epicardial monophasic AP recordings from the RV outflow tract (RVOT) in patients with BrS who were undergoing open chest surgery (*22*). This implies that the characteristic monophasic AP morphology recorded in BrS might be attributed to the selective decrease of $I_{Na,LM}$ in epicardial myocytes located in the RVOT.

Loss of $I_{Na,LM}$ causes the BrS loss-of-dome AP morphology

The loss of the AP dome and marked shortening of APD in epicardial myocytes in the RVOT, i.e., repolarization abnormality (*6*, *24*), are considered to be one of the mechanisms of coved-type ST-segment elevation (Brugada-type ECG) (*25*). One of the factors causing the loss-of-dome is thought to be the ventricular gradient of I_{to} through the RV wall, as well as endogenously heterogeneous I_{to} in the RV epicardial layers (*6*). We showed that the loss-of-dome type abbreviated AP was also caused by extremely decrease and/or loss of Na^+ channels from the LM of each myocyte, even without changing I_{to} (Figs. 2A*d* and 2B*a*; green lines). Indeed, the loss of $I_{Na,LM}$ further decreased the AP phase-0 amplitude, therefore preventing the V_m depolarization at AP phase-0 from reaching −30 mV, a threshold potential for I_{CaL} activation (see Fig. 2B*a*, green line); this thus failed to activate I_{CaL} (Fig. 2B*d*), resulting in the loss-of-dome type abbreviated AP (Fig. 2B*a*, green line). Based on the present simulation study, the loss of the AP dome can be also explained by both the I_{Kr} activation (Fig. 2B*g*, green line) and

bioRxiv preprint doi: https://doi.org/10.1101/805986; this version posted October 16, 2019. The copyright holder for this preprint (which was not certified by peer review) is the author/funder. All rights reserved. No reuse allowed without permission.

the earlier late peak (*) of I_{K1} (Fig. 2B*h*, green line), even without the activation of I_{to} (please note that the very small I_{to} was observed in Fig. 2B*c*). These results suggest that the Na^+ channel abnormality, which is commonly believed to be the cause of the depolarization abnormality in BrS (*24*), may also be responsible for the repolarization abnormality of BrS.

Selective decrease in $I_{Na,LM}$ causes the depolarization abnormality in BrS

We found that the conduction delay in RVOT under structurally normal hearts in patients with BrS (*26*), i.e., depolarization disorder hypothesis (*24*), may be attributable to the selective decrease in $I_{Na,LM}$ causing decreases in I_g without the G_g change. The mechanism of $I_{Na,LM}$-mediated decreases in I_g proposed in the present theoretical study is as follows: (1) The marked decrease in $I_{Na,LM}$ decreases the pre-JM current (compare left to right panels of fig. S2C) and thus slows the depolarization of the pre-JM (compare left to right panels of fig. S2D). (2) The slower and smaller depolarization of the pre-JM due to the reduced pre-JM current leads to decreases in the difference between $V_{i,\mathrm{pre-JM}}^{k}$ and $V_{i,\mathrm{post-JM}}^{k+1}$, for k = 1, 2,..., 299, resulting in the I_g decrease. This notion is also supported by previous experimental studies (*9*, *10*), which showed that mutant mice hearts with a selective decrease in Na^+ channel expression at the LM had slower CV than the wild type, without affecting the connexin 43 (Cx43; gap-junction channel-forming proteins) expression (table S3).

Possible mechanisms of P2R and related arrhythmias

The underlying mechanism of P2R is commonly explained by the electrotonic interaction between the region with normal AP morphology and the adjacent region

bioRxiv preprint doi: https://doi.org/10.1101/805986; this version posted October 16, 2019. The copyright holder for this preprint (which was not certified by peer review) is the author/funder. All rights reserved. No reuse allowed without permission.

with the loss of the AP dome. Such P2R mechanism were explored in numerous experimental (*27*, *28*) and computational studies (*29-31*). For the onset of P2R, excitable tissues such as RV and RVOT, in general, are required to be separated into two regions by the segment of reduced excitability and/or reduced electrical coupling. The existence of a local difference in AP waveform (or local APD difference) at the RVOT epicardium has been confirmed by several experimental studies (*8*, *32*). Our results showed that an existence of the slight spatial heterogeneity at tissue-level in Na^+ channel expressions accompanied by a marked decrease in $I_{Na,LM}$ (reduced excitability) could induce P2R (Fig. 3). Although the causes that make the local differences of APs in the RVOT/RV are not clear, one possible cause is an endogenous heterogeneity in Na^+ channel expression at the RVOT epicardial layer as in the transmural difference in Na^+ channel expression in the RVOT and the RV free wall (*33*). On the other hand, Auerbach and co-workers (*34*) have shown by combined experimental and computational studies that a structural heterogeneity (a geometric expansion) can produce P2R. In addition to differences in electrophysiological properties due to differences in the developmental origin of the RVOT and RV (*35*), a tissue structure of the RVOT with more aligned fiber orientations is different from that of the RV free wall which comprised of network-like structures of myocardial fibers; the structural heterogeneity between the RV free wall and RVOT might be also responsible for the P2R development in patients with BrS.

A recent clinical observation (*36*) has demonstrated that BrS is associated with epicardial interstitial fibrosis and reduced Cx43 expression in the RVOT. Furthermore, previous experimental studies using the *Scn5a* heterozygous (*Scn5a*+/-) mice (*37*, *38*) have shown that fibrosis, accompanied by downregulation and redistribution of Cx43, is

bioRxiv preprint doi: https://doi.org/10.1101/805986; this version posted October 16, 2019. The copyright holder for this preprint (which was not certified by peer review) is the author/funder. All rights reserved. No reuse allowed without permission.

increased with aging. The I_g decrease with G_g change leads to a decrease in the local current ($I_{m,LM}$) consisting of I_g and $I_{m,post\text{-}JM}$ (figs. S2B and S2E). Besides $I_{Na,LM}$ reduction, decreases in I_g could result in the loss-of-dome abbreviated AP (*31*). Therefore, we speculate that the decrease in gap junctions at the RVOT, where Na^+ channel expression is impaired along with aging-associated fibrosis, may also cause the loss of the AP dome followed by P2R resulting in VT/VF.

Contribution of I_{CaL} to P2R

Miyoshi et al (*30*) suggested that I_{CaL} plays critical roles in the formation of local APD differences even during AP propagation and the following second excitation during P2R. Indeed, as shown in Figs. 2B and 4B, I_{CaL} was the main determinant of AP dome formation in each myocyte of the myocardial strand. As the original ORd model was constrained as AP behaviors observed in the human left ventricular endocardial myocyte, actual I_{CaL} in the RVOT might be different from that in the left ventricular myocyte. In the present study, we increased the I_{CaL} by 30% from the original value in the ORd model (*16*) to reproduce P2R development. This modification was needed to maintain the second excitation wave propagation during P2R, consequently leading to reentrant excitation wave propagations (VT/VF) in a myocardial ring model (Fig. 6). On the other hand, it is known that the sympathetic activation in patients with BrS decreases VT/VF initiation (*39*), predicting that the greater I_{CaL} enhancement contributes to preventing P2R. We demonstrated that β-AS by the administration of isoproterenol could reduce the local APD difference and could prevent P2R (Fig. 5); more quantitative experimental verification and theoretical studies using more elaborate intracellular Ca^{2+}-signaling models (*40*) are required to understand the exact roles of

bioRxiv preprint doi: https://doi.org/10.1101/805986; this version posted October 16, 2019. The copyright holder for this preprint (which was not certified by peer review) is the author/funder. All rights reserved. No reuse allowed without permission.

I_{CaL} modulation by β-AS in P2R and arrhythmia preventions. Furthermore, additional simulations employing more sophisticated, three-dimensional, whole ventricle models will be needed to elucidate the roles of the loss-of-function of Na^+ channels in BrS.

Supplementary Materials

Materials and Methods

Fig. S1. Myocardial strand model and its equivalent circuit

Fig. S2. Effect of I_{Na} changes in the lateral membrane (LM) on conduction velocity (CV)

Fig. S3. Overview of simulated AP propagation in myocardial ring models with spatially-heterogeneous Na^+ channel distributions

Table S1. Control parameter values

Table S2. Modification parameters for the condition of β-adrenergic stimulation (β-AS)

Table S3. Comparison with experimental results in ΔSIV mice

bioRxiv preprint doi: https://doi.org/10.1101/805986; this version posted October 16, 2019. The copyright holder for this preprint (which was not certified by peer review) is the author/funder. All rights reserved. No reuse allowed without permission.

References and Notes:

1. H. Abriel, Cardiac sodium channel Na(v)1.5 and interacting proteins: Physiology and pathophysiology. *J Mol Cell Cardiol* **48**(1), 2−11 (2010).
2. Q. Chen, G. E. Kirsch, D. Zhang, R. Brugada, J. Brugada, P. Brugada, D. Potenza, A. Moya, M. Borggrefe, G. Breithardt, R. Ortiz-Lopez, Z. Wang, C. Antzelevitch, R. E. O'Brien, E. Schulze-Bahr, M. T. Keating, J. A. Towbin, Q. Wang, Genetic basis and molecular mechanism for idiopathic ventricular fibrillation. *Nature* **392**(6673),293−296 (1998).
3. S.L. Van Driest, Q. S. Wells, S. Stallings, W. S. Bush, A. Gordon, D. A. Nickerson, J. H. Kim, D. R. Crosslin, G. P. Jarvik, D. S. Carrell, J. D. Ralston, E. B. Larson, S. J. Bielinski, J. E. Olson, Z. Ye, I. J. Kullo, N. S. Abul-Husn, S. A. Scott, E. Bottinger, B. Almoguera, J. Connolly, R. Chiavacci, H. Hakonarson, L. J. Rasmussen-Torvik, V. Pan, S. D. Persell, M. Smith, R. L. Chisholm, T. E. Kitchner, M. M. He, M. H. Brilliant, J. R. Wallace, K. F. Doheny, M. B. Shoemaker, R. Li, T. A. Manolio, T. E. Callis, D. Macaya, M. S. Williams, D. Carey, J. D. Kapplinger, M. J. Ackerman, M. D. Ritchie, J. C. Denny, D. M. Roden, Association of Arrhythmia-Related Genetic Variants With Phenotypes Documented in Electronic Medical Records. *JAMA* **315**(1), 47−57 (2016).
4. P. Brugada, J. Brugada, Right bundle branch block, persistent ST segment elevation and sudden cardiac death: a distinct clinical and electrocardiographic syndrome. A multicenter report. *J Am Coll Cardiol* **20**(6), 1391−1396 (1992).
5. F. Sendfeld, E. Selga, F. S. Scornik, G. J. Pérez, N. L. Mills, R. Brugada, Experimental Models of Brugada syndrome. *Int J Mol Sci* **20**(9). pii:E2123 (2019). doi: 10.3390/ijms20092123.
6. C. Antzelevitch, The Brugada syndrome: ionic basis and arrhythmia mechanisms. *J Cardiovasc Electrophysiol* **12**(2), 268−272 (2001).
7. T. Aiba, W. Shimizu, I. Hidaka, K. Uemura, T. Noda, C. Zheng, A. Kamiya, M. Inagaki, M. Sugimachi, K. Sunagawa, Cellular basis for trigger and maintenance of ventricular fibrillation in the Brugada syndrome model: high-resolution optical mapping study. *J Am Coll Cardiol* **47**(10), 2074−2085 (2006).
8. H. Morita, D. P. Zipes, K. Fukushima-Kusano, S. Nagase, K. Nakamura, S. T. Morita, T. Ohe, J. Wu, Repolarization heterogeneity in the right ventricular outflow tract: correlation with ventricular arrhythmias in Brugada patients and in an in vitro canine Brugada model. *Heart Rhythm* **5**(5), 725−733 (2008).
9. S. Petitprez, A. F. Zmoos, J. Ogrodnik, E. Balse, N. Raad, S. El-Haou, M. Albesa, P. Bittihn, S. Luther, S. E. Lehnart, S. N. Hatem, A. Coulombe, H. Abriel, SAP97 and dystrophin macromolecular complexes determine two pools of cardiac sodium channels Nav1.5 in cardiomyocytes *Circ Res* **108**(3), 294−304 (2011).
10. D. Shy, L. Gillet, J. Ogrodnik, M. Albesa, A. O. Verkerk, R. Wolswinkel, J. S. Rougier, J. Barc, M. C. Essers, N. Syam, R. F. Marsman, A. M. van Mil, S. Rotman, R. Redon, C. R. Bezzina, C. A . Remme, H. Abriel, PDZ domain-binding motif regulates cardiomyocyte compartment-specific NaV1.5 channel expression and function. *Circulation* **130**(2), 147−160 (2014).

bioRxiv preprint doi: https://doi.org/10.1101/805986; this version posted October 16, 2019. The copyright holder for this preprint (which was not certified by peer review) is the author/funder. All rights reserved. No reuse allowed without permission.

11. K. Tsumoto, T. Ashihara, R. Haraguchi, K. Nakazawa, Y. Kurachi, Ischemia-related subcellular redistribution of sodium channels enhances the proarrhythmic effect of class I antiarrhythmic drugs: a simulation study. *PLoS One* **9**(10), e109271 (2014).
12. L. Virág, N. Iost, M. Opincariu, J. Szolnoky, J. Szécsi, G. Bogáts, P. Szenohradszky, A. Varró, J. G. Papp, The slow component of the delayed rectifier potassium current in undiseased human ventricular myocytes. *Cardiovasc Res* **49**(4), 790−797 (2001).
13. J. P. Kucera, S. Rohr, Y. Rudy, Localization of sodium channels in intercalated disks modulates cardiac conduction. *Circ Res* **91**(12), 1176−1182 (2002).
14. Y. Mori, G. I. Fishman, C. S. Peskin, Ephaptic conduction in a cardiac strand model with 3D electrodiffusion. *Proc Natl Acad Sci U S A* **105**(17), 6463−6468 (2008).
15. S. A. Cohen, Immunocytochemical localization of rH1 sodium channel in adult rat heart atria and ventricle. Presence in terminal intercalated disks. *Circulation* **94**(12), 3083−3086 (1996).
16. T. O'Hara, L. Virág, A. Varró, Y. Rudy, Simulation of the undiseased human cardiac ventricular action potential: model formulation and experimental validation. *PLoS Comput Biol* **7**(5), e1002061 (2011).
17. K. Furutani, K. Tsumoto, I. S. Chen, K. Handa, Y. Yamakawa, J. T. Sack, Y. Kurachi, Facilitation of I_{Kr} current by some hERG channel blockers suppresses early afterdepolarizations. *J Gen Physiol* **151**(2), 214−230 (2019). doi: 10.1085/jgp.201812192.
18. P. Taggart, P. M. Sutton, T. Opthof, R. Coronel, R. Trimlett, W. Pugsley, P. Kallis, Inhomogeneous transmural conduction during early ischaemia in patients with coronary artery disease. *J Mol Cell Cardiol* **32**(4), 621−630 (2000).
19. K. H. ten Tusscher, A. V. Panfilov, Alternans and spiral breakup in a human ventricular tissue model. *Am J Physiol Heart Circ Physiol* **291**(3), H1088−H1100 (2006).
20. J. Zeng, Y. Rudy, Early afterdepolarizations in cardiac myocytes: mechanism and rate dependence. *Biophys J* **68**(3), 949−964 (1995).
21. Y. Kurata, K. Tsumoto, K. Hayashi, I. Hisatome, M. Tanida, Y. Kuda, T. Shibamoto, Dynamical mechanisms of phase-2 early afterdepolarizations in human ventricular myocytes: insights from bifurcation analyses of two mathematical models. *Am J Physiol Heart Circ Physiol* **312**(1), H106−H127 (2017). doi: 10.1152/ajpheart.00115.2016.
22. T. Kurita, W. Shimizu, M. Inagaki, K. Suyama, A. Taguchi, K. Satomi, N. Aihara, S. Kamakura, J. Kobayashi, Y. Kosakai, The electrophysiologic mechanism of ST-segment elevation in Brugada syndrome. *J Am Coll Cardiol* **40**(2), 330−334 (2002).
23. R. Coronel, S. Casini, T. T. Koopmann, F. J. Wilms-Schopman, A. O. Verkerk, J. R. de Groot, Z. Bhuiyan, C. R. Bezzina, M. W. Veldkamp, A. C. Linnenbank, A. C. van der Wal, H. L. Tan, P. Brugada, A. A. Wilde, J. M. de Bakker, Right ventricular fibrosis and conduction delay in a patient with clinical signs of Brugada syndrome:

bioRxiv preprint doi: https://doi.org/10.1101/805986; this version posted October 16, 2019. The copyright holder for this preprint (which was not certified by peer review) is the author/funder. All rights reserved. No reuse allowed without permission.

a combined electrophysiological, genetic, histopathologic, and computational study. *Circulation* **112**(18), 2769−2777 (2005).

24. P. G. Meregalli, A. A. Wilde, H. L. Tan, Pathophysiological mechanisms of Brugada syndrome: depolarization disorder, repolarization disorder, or more? *Cardiovasc Res* **67**(3), 367−378 (2005).
25. R. Brugada, J. Brugada, C. Antzelevitch, G. E. Kirsch, D. Potenza, J. A. Towbin, P. Brugada, Sodium channel blockers identify risk for sudden death in patients with ST-segment elevation and right bundle branch block but structurally normal hearts. *Circulation* **101**(5), 510−515 (2000).
26. S. Nagase, K. F. Kusano, H. Morita, Y. Fujimoto, M. Kakishita, K. Nakamura, T. Emori, H. Matsubara, T. Ohe, Epicardial electrogram of the right ventricular outflow tract in patients with the Brugada syndrome: using the epicardial lead. *J Am Coll Cardiol* **39**(12), 1992−1995 (2002).
27. J. Davidenko, C. Antzelevitch, The effects of milrinone on action potential characteristics, conduction, automaticity, and reflected reentry in isolated myocardial fibers. *J Cardiovasc Pharmacol* **7**(2), 341−349 (1985).
28. A. Lukas, C. Antzelevitch, Phase 2 reentry as a mechanism of initiation of circus movement reentry in canine epicardium exposed to simulated ischemia. *Cardiovasc Res* **32**(3), 593−603 (1996).
29. C. Cabo, R. C. Barr, Reflection after delayed excitation in a computer model of a single fiber. *Circ Res* **71**(2), 260−270 (1992).
30. S. Miyoshi, H. Mitamura, K. Fujikura, Y. Fukuda, K. Tanimoto, Y. Hagiwara, M. Ita, S. Ogawa, A mathematical model of phase 2 reentry: role of L-type Ca current. *Am J Physiol Heart Circ Physiol* **284**(4), H1285−H1294 (2003).
31. A. Bueno-Orovio, E. M. Cherry, S. J. Evans, F. H. Fenton, Basis for the induction of tissue-level phase-2 reentry as a repolarization disorder in the Brugada syndrome. *Biomed Res Int* **2015**, 197586 (2015). doi: 10.1155/2015/197586.
32. M. Kimura, T. Kobayashi, S. Owada, K. Ashikaga, T. Higuma, S. Sasaki, A. Iwasa, S. Motomura, K. Okumura, Mechanism of ST elevation and ventricular arrhythmias in an experimental Brugada syndrome model. *Circulation* **109**(1), 125−131 (2004).
33. G. Szabó, N.Szentandrássy, T. Bíró, B. I. Tóth, G. Czifra, J. Magyar, T. Bányász, A. Varró, L. Kovács, P. P. Nánási, Asymmetrical distribution of ion channels in canine and human left-ventricular wall: epicardium versus midmyocardium. *Pflugers Arch* **450**(5), 307−316 (2005).
34. D. S. Auerbach, K. R. Grzda, P. B. Furspan, P. Y. Sato, S. Mironov, J. Jalife, Structural heterogeneity promotes triggered activity, reflection and arrhythmogenesis in cardiomyocyte monolayers. *J Physiol* **589**(Pt 9), 2363−2381 (2011). doi: 10.1113/jphysiol.2010.200576.
35. B. J. Boukens, V. M. Christoffels, R. Coronel, A. F. Moorman, Developmental basis for electrophysiological heterogeneity in the ventricular and outflow tract myocardium as a substrate for life-threatening ventricular arrhythmias. *Circ Res* **104**(1), 19−31 (2009).

bioRxiv preprint doi: https://doi.org/10.1101/805986; this version posted October 16, 2019. The copyright holder for this preprint (which was not certified by peer review) is the author/funder. All rights reserved. No reuse allowed without permission.

36. K. Nademanee, H. Raju, S. V. de Noronha, M. Papadakis, L. Robinson, S. Rothery, N. Makita, S. Kowase, N. Boonmee, V. Vitayakritsirikul, S. Ratanarapee, S. Sharma, A. C. van der Wal, M. Christiansen, H. L. Tan, A. A. Wilde, A. Nogami, M. N. Sheppard, G. Veerakul, E. R. Behr, Fibrosis, Connexin-43, and Conduction Abnormalities in the Brugada Syndrome. *J Am Coll Cardiol* **66**(18), 1976−1986 (2015).

37. T. A. van Veen, M. Stein, A. Royer, K. Le Quang, F. Charpentier, W. H. Colledge, C. L. Huang, R. Wilders, A. A. Grace, D. Escande, J. M. de Bakker, H. V. van Rijen, Impaired impulse propagation in Scn5a-knockout mice: combined contribution of excitability, connexin expression, and tissue architecture in relation to aging. *Circulation* **112**(13), 1927−1935 (2005).

38. J.A. Jansen, M. Noorman, H. Musa, M. Stein, S. de Jong, R. van der Nagel, T. J. Hund, P. J. Mohler, M. A. Vos, T. A. van Veen, J. M. de Bakker, M. Delmar, H. V. van Rijen, Reduced heterogeneous expression of Cx43 results in decreased Nav1.5 expression and reduced sodium current that accounts for arrhythmia vulnerability in conditional Cx43 knockout mice. *Heart Rhythm* **9**(4), 600−607 (2012).

39. A. Watanabe, K. Fukushima Kusano, H. Morita, D. Miura, W. Sumida, S. Hiramatsu, K. Banba, N. Nishii, S. Nagase, K. Nakamura, S. Sakuragi, T. Ohe, Low-dose isoproterenol for repetitive ventricular arrhythmia in patients with Brugada syndrome. *Eur Heart J* **27**(13), 1579−1583 (2006).

40. J. Heijman, P. G. Volders, R. L. Westra, Y. Rudy, Local control of β-adrenergic stimulation: Effects on ventricular myocyte electrophysiology and Ca^{2+}-transient. *J Mol Cell Cardiol* **50**(5), 863−871 (2011). doi: 10.1016/j.yjmcc.2011.02.007.

Funding: This work was supported by grants from the Japan Society for the Promotion of Science (JSPS) KAKENHI Grant Numbers 24790214 and 16KT0194, The Takeda Science Foundation (to K.T.), the Hiroshi and Aya Irisawa Memorial Promotion Award for Young Physiologists from the Physiological Society of Japan (to K.T.), and Grant for Promoted Research (S2019-2) from Kanazawa Medical University (to K.T.), and the Japanese Ministry of Education, Culture, Sports, Science and Technology (MEXT) KAKENHI Grant Number 22136002 (to Yo.K.). **Author contributions**: K.T., T.A. and Yo.K. conceived and designed the experiments; K.T., N.N., and T.S. conducted the simulations, performed numerical calculations and prepared figures; K.T., T.A. N.N., T.S., Ya.K., and Yo.K. analyzed and interpreted results; K.T., T.A., Ya.K., A.A. and Yo.K. drafted and edited the manuscript. All authors reviewed and approved the final version of manuscript. Competing interests: The authors declare no competing financial interests. **Data and materials availability**: These simulation codes of the myocardial strand and ring models are available on the author's GitHub site: https://github.com/92tsumoto/BrS-P2R-strand-ORd2011model-withTNNP_INa-FT_IKr, and https://github.com/92tsumoto/BrS-P2R-ring-ORd2011model-withTNNP_INa-FT_IKr.

bioRxiv preprint doi: https://doi.org/10.1101/805986; this version posted October 16, 2019. The copyright holder for this preprint (which was not certified by peer review) is the author/funder. All rights reserved. No reuse allowed without permission.

Figures:

Fig. 1. Myocardial strand and ring models. A and **B**, Schematic representation of a myocardial strand model comprising cylindrical 300 cells (*a*) and of intercellular junction between myocytes (*b*). The cell membrane in each myocyte is divided into post-junctional, lateral, and pre-junctional segments, and electrophysiological properties of the each membrane segment are represented by a modified O'Hara-Rudy dynamic (mORd) ventricular myocyte model (*c*) (*16*, *17*). **B**, Schematic representations of the myocardial ring model comprising 600 cells. Cell #1 (A) and #300 (B) were electrically stimulated at 1 Hz. G_g, gap junction conductance; G_j, radial conductance of intercellular cleft; G_d, axial conductance of intercellular cleft.

Fig. 2. Effects of the subcellular Na^+ channel distribution on action potential (AP) morphology and conduction velocity (CV). A, AP propagation observed in the myocardial strand model with a spatially-homogeneous reduction in Na^+ channel conductance in the lateral membrane (LM) of 100%$g_{Na,LM}$ (*a*), 35%$g_{Na,LM}$ (*b*), 7%$g_{Na,LM}$ (*c*), and 0%$g_{Na,LM}$ (*d*). **B**, AP morphological changes (*a*), I_{Na} at the LM, $I_{Na,LM}$ (*b*), I_{to} (*c*), I_{CaL} (*d*), I_{NaK} (*e*), I_{Ks} (*f*), I_{Kr} (*g*), and I_{K1} (*h*) at the LM. The APs and ion currents were recorded in a myocyte located at the middle of the myocardial strand (cell #150). Each AP morphology corresponds to the waveforms in panel (A) indicated by red, cyan, blue, and green lines. CVs at 100%$g_{Na,LM}$, 35%$g_{Na,LM}$, 7%$g_{Na,LM}$ and 0%$g_{Na,LM}$ were 71.4, 53.6, 33.3, and 25.4 cm/s, respectively (see Table 1).

Fig. 3. Simulated phase-2 reentry (P2R) development in the strand model. A, Examples of typical patterns of AP propagation observed in the myocardial strand model with a spatially-heterogeneous Na^+ channel distribution on the LM of 7%$g_{Na,LM}$ in the distal (cell #201-300) and smaller %$g_{Na,LM}$ in the proximal (cell #1-200): AP alternans (AL) (*a*) and 2:1 retrograde P2R (*b*) at 6% and 4%$g_{Na,LM}$, respectively, in the proximal. Arrows and black short bars indicate the direction of AP propagation and blockage, respectively. **B**, A phase diagram of AP propagation patterns for the %$g_{Na,LM}$ in proximal myocytes vs. %$g_{Na,LM}$ in distal myocytes. Open circles labeled as *a* and *b* correspond to the parameter sets

bioRxiv preprint doi: https://doi.org/10.1101/805986; this version posted October 16, 2019. The copyright holder for this preprint (which was not certified by peer review) is the author/funder. All rights reserved. No reuse allowed without permission.

for A(*a*) and A(*b*). RC and IC indicate AP propagation with regular pattern and irregular one, respectively.

Fig. 4. Mechanism of phase-2 reentry (P2R). A, The simulated AP propagation in the myocardial strand model during the development of 2:1 P2R shown in Fig. 3A*b*. **B**, Simulated behaviors of the membrane potential (V_m) in several myocytes (#140-260) during the 2:1 P2R development. **C**, The gap junctional currents, I_g, flowing from the cell #140 to #260. **D**, I_{Na} in the post-junctional membrane ($I_{Na,post\text{-}JM}$) (*a*), the lateral membrane ($I_{Na,LM}$) (*b*), and the pre-junctional membrane ($I_{Na,pre\text{-}JM}$) (*c*). **E**, I_{CaL} (*a*), I_{to} (*b*), I_{Kr} (*c*), and I_{K1} (*d*) during the P2R development.

Fig. 5. Mechanisms for the prevention of phase-2 reentry (P2R) under *β*-AS condition. A and **B**, The simulated AP propagation (A) and the membrane potential (V_m) change (B) of several myocytes in the myocardial strand model under the same condition as for Fig. 3A*b* but during *β*-AS. **C-E**, The gap junctional current, I_g (C), I_{Na} in the post-junctional membrane (JM), $I_{Na,post\text{-}JM}$ (D*a*), I_{Na} in the lateral membrane, $I_{Na,LM}$ (D*b*), and I_{Na} in the pre-JM, $I_{Na,pre\text{-}JM}$ (D*c*), I_{CaL} (E*a*), I_{to} (E*b*), I_{Kr} (E*c*), and I_{K1} (E*d*) during *β*-AS.

Fig. 6. Rotatory reentry induction in the myocardial ring model. A, The simulated AP propagation in the myocardial ring with spatially-homogeneous Na^+ channel distribution with 10%$g_{Na,LM}$ (*a*) and 5%$g_{Na,LM}$ (*b*) in the lateral membrane (LM) segment of each myocyte. **B**, The simulated AP propagation in the same model but with a spatially-heterogeneous Na^+ channel distribution with 5%$g_{Na,LM}$ in the LM of the 1st to 100th myocytes and 3%$g_{Na,LM}$ (*a*) and 2%$g_{Na,LM}$ (*b*) in the LM of the 101st to 600th myocytes. Arrows and black short bars indicate the direction of AP propagation and blockage, respectively. Asterisks and dagger symbols represent the collision of excitation wavefronts, and the blockade of AP propagation, respectively. The red trace represents the AP behavior at the stimulus site (cell #300).

bioRxiv preprint doi: https://doi.org/10.1101/805986; this version posted October 16, 2019. The copyright holder for this preprint (which was not certified by peer review) is the author/funder. All rights reserved. No reuse allowed without permission.

Table 1. Relationships of the Na^+ channel density at the lateral membrane, the regional Na^+ channel current, and conduction velocity

	100%$g_{Na,LM}$	**35%$g_{Na,LM}$**	**7%$g_{Na,LM}$**	**0%$g_{Na,LM}$**
Peak $I_{Na,LM}$ (pA/pF)	329.3	138.7	24.6	0.0
CV (cm/s)	71.4	53.6	33.3	25.4

%$g_{Na,LM,}$, a percent g_{Na} in the lateral membrane (LM) segment of each cell of the strand model; Peak $I_{Na,LM}$, peak value of I_{Na} across the LM segment of the 150th cell in the myocardial strand model; CV, conduction velocity.

Table 2. Effects of changes in Na^+ channel density of the lateral membrane on epicardial action potential parameters

	100%$g_{Na,LM}$	**35%$g_{Na,LM}$**	**7%$g_{Na,LM}$**	**0%$g_{Na,LM}$**
APD_{90} (ms)	240.0	235.2	258.5	136.3
$\dot{V}_{max}$ (mV/ms)	238.8	96.1	39.0	26.9
RMP (mV)	−87.7	−87.7	−87.7	−87.8
AAP (mV)	124.6	124.4	118.3	52.5

Each parameter is determined for the LM segment of the 150th cell in the myocardial strand model comprised of 300 epicardial ventricular myocytes. APD_{90}, action potential duration measured at 90% repolarization; $\dot{V}_{max}$, maximum upstroke velocity of action potential; RMP, resting membrane potential; AAP, amplitude of action potential.

bioRxiv preprint doi: https://doi.org/10.1101/805986; this version posted October 16, 2019. The copyright holder for this preprint (which was not certified by peer review) is the author/funder. All rights reserved. No reuse allowed without permission.

Supplementary Materials

Expanded Methods

Myocardial strand and ring models

We constructed myocardial strand and ring models comprising 300 (Fig. 1A) and 600 ventricular myocytes (Fig. 1D), respectively. As with our previous study (*11*), the cytosolic conductance (G_i) of each myocyte was 2.327 μS, calculated from $G_i = \sigma_{myo} \cdot \pi \cdot r^2/l$, where σ_{myo} (11.1 mS/cm) is the cytosolic conductivity, and l (150 μm) and r (10 μm) are the length and radius of the myocyte, respectively (*12*). In addition, the radial cleft conductance (G_j) and series axial cleft conductance (G_d) were defined as $G_j = 8 \cdot \pi \cdot w \cdot \sigma_{ext}$ and $G_d = \sigma_{ext} \cdot \pi \cdot r^2/w$, respectively (*13*, *14*), where σ_{ext} (6.7 mS/cm) is the extracellular conductivity, and w (15 nm) is the cleft width, which is the distance between the pre- (pre-JM) and post-junctional membrane (post-JM), as an averaged value (*11*, *13*).

Electrophysiological properties of each membrane segment composing the ventricular myocyte were described by a modified O'Hara–Rudy dynamic (mORd) model (*16*). The mORd model consisted of a membrane capacitance and several ion channel currents, including our modification (*17*) to the original currents of a potassium channel (I_{Kr}). Furthermore, the fast I_{Na} in the original ORd model was replaced with that of the ten Tusscher-Panfilov (TP) model (*19*). From experimental data (*12*), the entire membrane capacitance of a human ventricular myocyte was set to 185 pF ($C_{m,post\text{-}JM} = C_{m,pre\text{-}JM} = 5.8$ pF; $C_{m,LM} = 173.4$ pF) and the initial value of $[Na^+]_i$ was set to 7.0 mM. Table S1 shows the modification parameters of the relevant models.

Calculations

The calculation methods for action potential propagation in the myocardial strand and ring models are as follows. From the equivalent circuits of the myocyte model shown in Fig. S1, let us give the following current vector (**I**) comprised of the transmembrane current from each node toward each membrane segment:

$$\mathbf{I} = \left[i_{m,1}^{1} \quad i_{m,2}^{1} \quad \cdots \quad i_{m,3}^{k-1} \quad \middle| i_{m,1}^{k} \quad i_{m,2}^{k} \quad i_{m,3}^{k} \middle| i_{m,1}^{k+1} \quad \cdots \quad i_{m,2}^{N} \quad i_{m,3}^{N} \right]^T, \qquad \text{(S1)}$$

where $[\ ]^T$ represents the transpose operation and N is the total myocyte number. Furthermore, we suppose that a vector (**V**) consisting of the functions of the transmembrane potential of each membrane segment is given by

bioRxiv preprint doi: https://doi.org/10.1101/805986; this version posted October 16, 2019. The copyright holder for this preprint (which was not certified by peer review) is the author/funder. All rights reserved. No reuse allowed without permission.

$$\mathbf{V} = \left[v_{1,1} \quad v_{1,2} \quad \cdots \quad v_{k-1,3} \;\middle|\; v_{k,1} \quad v_{k,2} \quad v_{k,3} \;\middle|\; v_{k+1,1} \quad \cdots \quad v_{N,2} \quad v_{N,3}\right]^T. \qquad \text{(S2)}$$

Then, each function, $v_{k,l}$, for $k = 1, \ldots, N$ and $l = 1$, 2, and 3, except for the first function ($v_{1,1}$) and the final one ($v_{N,3}$), in the voltage vector is given by

$$\begin{aligned} v_{k,1} &= 2G_i\left(V^k_{\mathrm{m,post-JM}} - V^k_{\mathrm{m,LM}}\right) - G_g\left(V^{k-1}_{\mathrm{m,pre-JM}} - V^k_{\mathrm{m,post-JM}}\right) \\ v_{k,2} &= -2G_i\left(V^k_{\mathrm{m,post-JM}} - 2V^k_{\mathrm{m,LM}} + V^k_{\mathrm{m,pre-JM}}\right) \\ v_{k,3} &= -2G_i\left(V^k_{\mathrm{m,LM}} - V^k_{\mathrm{m,pre-JM}}\right) + G_g\left(V^k_{\mathrm{m,pre-JM}} - V^{k+1}_{\mathrm{m,post-JM}}\right). \end{aligned} \qquad \text{(S3)}$$

In cases of $k = 1$ and $k = N$, $v_{1,1}$ and $v_{N,3}$ are provided by $v_{1,1} = 2G_i\left(V^1_{\mathrm{m,post-JM}} - V^1_{\mathrm{m,LM}}\right)$ and $v_{N,3} = -2G_i\left(V^N_{\mathrm{m,LM}} - V^N_{\mathrm{m,pre-JM}}\right)$, respectively. Using the current vector (Eq. S1) and the vector (Eq. S2), we can derive a linear equation at arbitrary time t using Ohm's law and Kirchhoff's law, leading to the following simultaneous equation:

$$\mathbf{RI}=\mathbf{V}, \qquad \text{(S4)}$$

where **R** is the $3N \times 3N$ matrix. The matrix, **R**, in Eq. S4 is given by Eq. S5:

$$\mathbf{R} = \left[\begin{array}{c|c|c|c|c}
\begin{matrix} -1 & & \\ & -1 & p_1 \\ & & p_3 \end{matrix} & \begin{matrix} p_2 & & \\ p_4 & & \end{matrix} & \mathbf{0} & \mathbf{0} & \mathbf{0} \\ \hline
\begin{matrix} & & \\ & p_4 & \\ & & \end{matrix} & \begin{matrix} p_3 & & \\ & \ddots & \\ & & p_3 \end{matrix} & \begin{matrix} & & \\ p_4 & & \\ & & \end{matrix} & \mathbf{0} & \mathbf{0} \\ \hline
\mathbf{0} & \begin{matrix} & & \\ & p_4 & \\ & p_2 & \end{matrix} & \begin{matrix} p_3 & & \\ p_1 & -1 & p_1 \\ & & p_3 \end{matrix} & \begin{matrix} p_2 & & \\ p_4 & & \\ & & \end{matrix} & \mathbf{0} \\ \hline
\mathbf{0} & \mathbf{0} & \begin{matrix} & & \\ & & \\ & p_4 & \end{matrix} & \begin{matrix} p_3 & & \\ & \ddots & \\ & & p_3 \end{matrix} & \begin{matrix} & & \\ p_4 & & \\ & & \end{matrix} \\ \hline
\mathbf{0} & \mathbf{0} & \mathbf{0} & \begin{matrix} & & \\ & p_4 & \\ & p_2 & \end{matrix} & \begin{matrix} p_3 & & \\ p_1 & -1 & \\ & & -1 \end{matrix}
\end{array}\right], \qquad \text{(S5)}$$

where $p_1 = 2G_i/G_j + G_i/G_d$, $p_2 = 2G_i/G_j$, $p_3 = -1.0 - 2G_i/G_j - G_i/G_d - 0.5\, G_g/G_d$, and $p_4 = -2G_i/G_j + 0.5\, G_g/G_d$. Equation S4 can be solved for the current $\boldsymbol{I}$ with $V^k_{\mathrm{m},l}$, for $l =$

bioRxiv preprint doi: https://doi.org/10.1101/805986; this version posted October 16, 2019. The copyright holder for this preprint (which was not certified by peer review) is the author/funder. All rights reserved. No reuse allowed without permission.

post-JM, LM, and pre-JM, at time t as an initial condition. Furthermore, in the case of the myocardial ring model, the following matrix was employed:

$$\mathbf{R} = \left[\begin{array}{ccc|ccc|ccc|ccc|ccc}
p_3 & & & & & & & & & & & & & & p_4 \\
p_1 & -1 & p_1 & p_2 & & & & \mathbf{0} & & & \mathbf{0} & & & & p_2 \\
 & & p_3 & p_4 & & & & & & & & & & & \\
\hline
 & & p_4 & p_3 & & & & & & & & & & & \\
 & & & & \ddots & & & & & & \mathbf{0} & & & \mathbf{0} & \\
 & & & & & p_3 & p_4 & & & & & & & & \\
\hline
 & & & & & p_4 & p_3 & & & & & & & & \\
 & \mathbf{0} & & & & p_2 & p_1 & -1 & p_1 & p_2 & & & & \mathbf{0} & \\
 & & & & & & & & p_3 & p_4 & & & & & \\
\hline
 & & & & & & & & p_4 & p_3 & & & & & \\
 & \mathbf{0} & & & \mathbf{0} & & & & & & \ddots & & & & \\
 & & & & & & & & & & & p_3 & p_4 & & \\
\hline
 & & & & & & & & & & & p_4 & p_3 & & \\
p_2 & & & & \mathbf{0} & & & \mathbf{0} & & & & p_2 & p_1 & -1 & p_1 \\
p_4 & & & & & & & & & & & & & & p_3
\end{array}\right], \quad \text{(S6)}$$

The transmembrane potential in each segment is given by

$$C_{\mathrm{m},l}\frac{\mathrm{d}V_{\mathrm{m},l}^{k}}{\mathrm{d}t} + I_{\mathrm{ion}}\left(V_{\mathrm{m},l}^{k}, t\right) = i_{\mathrm{m},l}^{k}, \qquad \text{(S7)}$$

for $k = 1, \ldots, N$ and l = post-JM, LM, and pre-JM, where $C_{\mathrm{m},l}$ (pF) is the membrane capacitance in each membrane segment, I_{ion} (μA/μF) is the sum of several ion channel currents in the mORd model, $i_{\mathrm{m},l}^{k}$ (μA/μF) is the transmembrane current corresponding to each element in the current vector defined by Eq. S1. For an arbitrary time t, all the membrane currents, $i_{\mathrm{m},l}^{k}$, are obtained by solving Eq. S4 with the transmembrane potentials as an initial condition. Thus, we calculated all transmembrane potentials at time $t+\Delta t$ in each segment, where Δt corresponds to the time step in the Euler method. The time step, Δt, was set to 1 μs. These codes used to simulate the myocardial strand and ring models are available in the repository: https://github.com/92tsumoto/BrS-P2R-strand-ORd2011model-withTNNP_INa-FT_IKr, and https://github.com/92tsumoto/BrS-P2R-ring-ORd2011model-withTNNP_INa-FT_IKr.

bioRxiv preprint doi: https://doi.org/10.1101/805986; this version posted October 16, 2019. The copyright holder for this preprint (which was not certified by peer review) is the author/funder. All rights reserved. No reuse allowed without permission.

Supplemental Figures

Fig. S1. Myocardial strand model and its equivalent circuit. Each membrane segment comprises a modified O'Hara-Rudy dynamic (mORd) model and membrane capacitance, $C_{\mathrm{m},l}$, for l = post-junctional membrane (post-JM), lateral membrane (LM), and pre-junctional membrane (pre-JM). V_{j}^{k} represents extracellular cleft potential just after the kth myocyte. $V_{\mathrm{i},l}^{k}$, and $V_{\mathrm{e},l}^{k}$, for l = post-JM, LM, and pre-JM, indicate the intracellular and extracellular potentials, respectively, of lth segment of the kth myocyte. $V_{\mathrm{m},l}^{k}$ denotes the transmembrane potential, i.e., $V_{\mathrm{m},l}^{k} = V_{\mathrm{i},l}^{k} - V_{\mathrm{e},l}^{k}$.

Fig. S2. Effect of I_{Na} changes in the lateral membrane (LM) on conduction velocity (CV). A, The schematic diagram of a intercellular junction part in the myocardial strand model. **B**, The post-junctional ($I_{\mathrm{m,post\text{-}JM}}$) and pre-junctional transmembrane currents ($I_{\mathrm{m,pre\text{-}JM}}$) in 150th myocyte. **C**, The transmembrane current ($I_{\mathrm{m,LM}}$) and I_{Na} in the LM segment of 150th myocytes. **D**, The intracellular potential (V_{i}) of the LM and pre-junctional membrane (pre-JM) in 150th myocyte, and of the post-junctional membrane (post-JM) in 151st myocyte. **E**, The gap junctional current (I_{g}) between the 150th and 151st myocytes.

Fig. S3. Overview of simulated AP propagation in myocardial ring models with spatially-heterogeneous Na^{+} channel distributions. A, 5%$g_{\mathrm{Na,LM}}$ in the LM of 1st to 100th myocytes and 3%$g_{\mathrm{Na,LM}}$ in the LM of 101st to 600th myocyte. **B**, 5%$g_{\mathrm{Na,LM}}$ in the LM of 1st to 100th myocytes and 2%$g_{\mathrm{Na,LM}}$ in the LM of 101st to 600th myocyte. Representations are the same as in Fig. 6.

bioRxiv preprint doi: https://doi.org/10.1101/805986; this version posted October 16, 2019. The copyright holder for this preprint (which was not certified by peer review) is the author/funder. All rights reserved. No reuse allowed without permission.

Supplemental Tables

Table S1. Control parameter values

Parameter	Definition	value
G_i	Myoplasmic conductance	2.327 μS
G_g	Intercellular gap junctional conductance	2.327 μS
G_j	Radial cleft conductance	0.25 μS
G_d	Axial cleft conductance	33.8 mS
$C_{m,pre\text{-}JM}$, $C_{m,post\text{-}JM}$	Capacitance of the pre- and post-junctional membranes	5.8 pF
$C_{m,LM}$	Capacitance of the lateral membrane	173.4 pF
$G_{NaF,pre\text{-}JM}$, $G_{NaF,post\text{-}JM}$	Maximum conductance density of fast Na^+ channel of the pre- and post-junctional membranes	44 nS/pF
$G_{NaF,LM}$	Maximum conductance density of fast Na^+ channel of the lateral membrane	11 nS/pF
$G_{NaL,pre\text{-}JM}$, $G_{NaL,post\text{-}JM}$	Maximum conductance density of late Na^+ channel of the pre- and post-junctional membranes	0.03 nS/pF
$G_{NaL,LM}$	Maximum conductance density of late Na^+ channel of the lateral membrane	0.0075 nS/pF
G_{kr}	Maximum conductance density of rapidly activating delayed rectifier K^+ channel	0.058 nS/pF
P_{Ca}	Ca^{2+} permeability for the L-type Ca^{2+} channel	0.00013 cm/s

JM, junctional membrane; LM, lateral membrane

bioRxiv preprint doi: https://doi.org/10.1101/805986; this version posted October 16, 2019. The copyright holder for this preprint (which was not certified by peer review) is the author/funder. All rights reserved. No reuse allowed without permission.

Table S2. Modification parameters for the condition of β-adrenergic stimulation (β-AS).

Parameter	**Control**	**β-AS (×ratio)**
Ca^{2+} permeability for the L-type Ca^{2+} channel (P_{Ca})	0.00013 cm/s	×3.0
Maximum conductance (G_{Ks}) of slowly activating delayed rectifier K^+ channel current (I_{Ks})	0.00476 nS/pF	×2.0
Maximum Na^+-K^+ pump current (I_{NaK})	27 pA/pF	×1.2
Maximum rate of Ca^{2+} uptake to SR	1.3 mM/ms	×1.41
Half-activation voltage in I_{Ks} activation gate	−11.6 mV	−19.6 mV

Table S3. Comparison with experimental results in ΔSIV mice

		100%$g_{Na,LM}$ (WT)	**35%$g_{Na,LM}$** (ΔSIV)	
Peak $I_{Na,LM}$ (pA/pF)	Tsumoto et al	329.3	138.7	57.9 % ↓
	Shy et al (*10*)	301.1 ± 25.4	115.0 ± 11.9	61.8 ± 4.0 % ↓
CV (cm/s)	Tsumoto et al	71.4	53.6	24.9 % ↓
	Shy et al (*10*)	70.1 ± 4.4	54.2 ± 2.9	22.7 ± 0.7 % ↓

Tsumoto et al, Present Study; Shy et al, (*10*)

bioRxiv preprint doi: https://doi.org/10.1101/805986; this version posted October 16, 2019. The copyright holder for this preprint (which was not certified by peer review) is the author/funder. All rights reserved. No reuse allowed without permission.

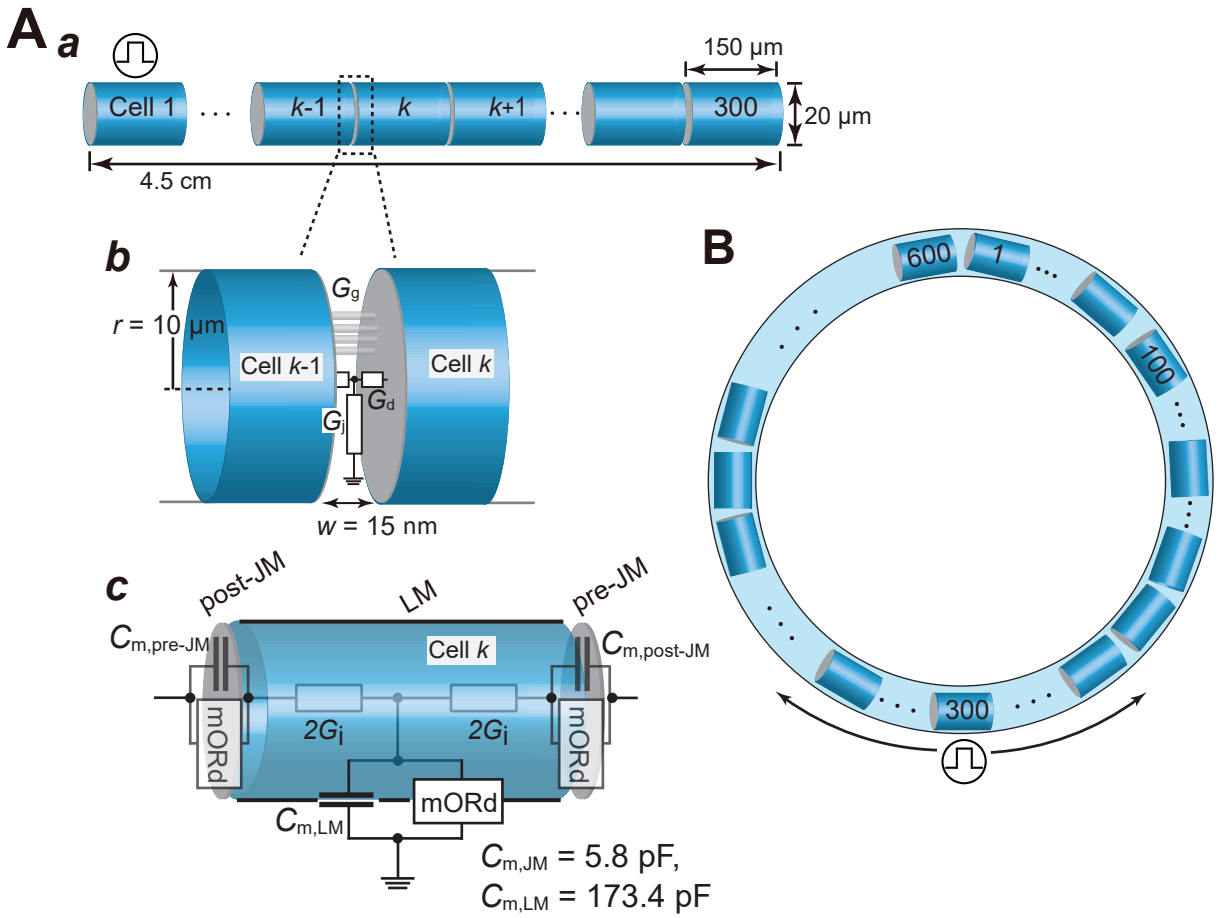

Figure 1

bioRxiv preprint doi: https://doi.org/10.1101/805986; this version posted October 16, 2019. The copyright holder for this preprint (which was not certified by peer review) is the author/funder. All rights reserved. No reuse allowed without permission.

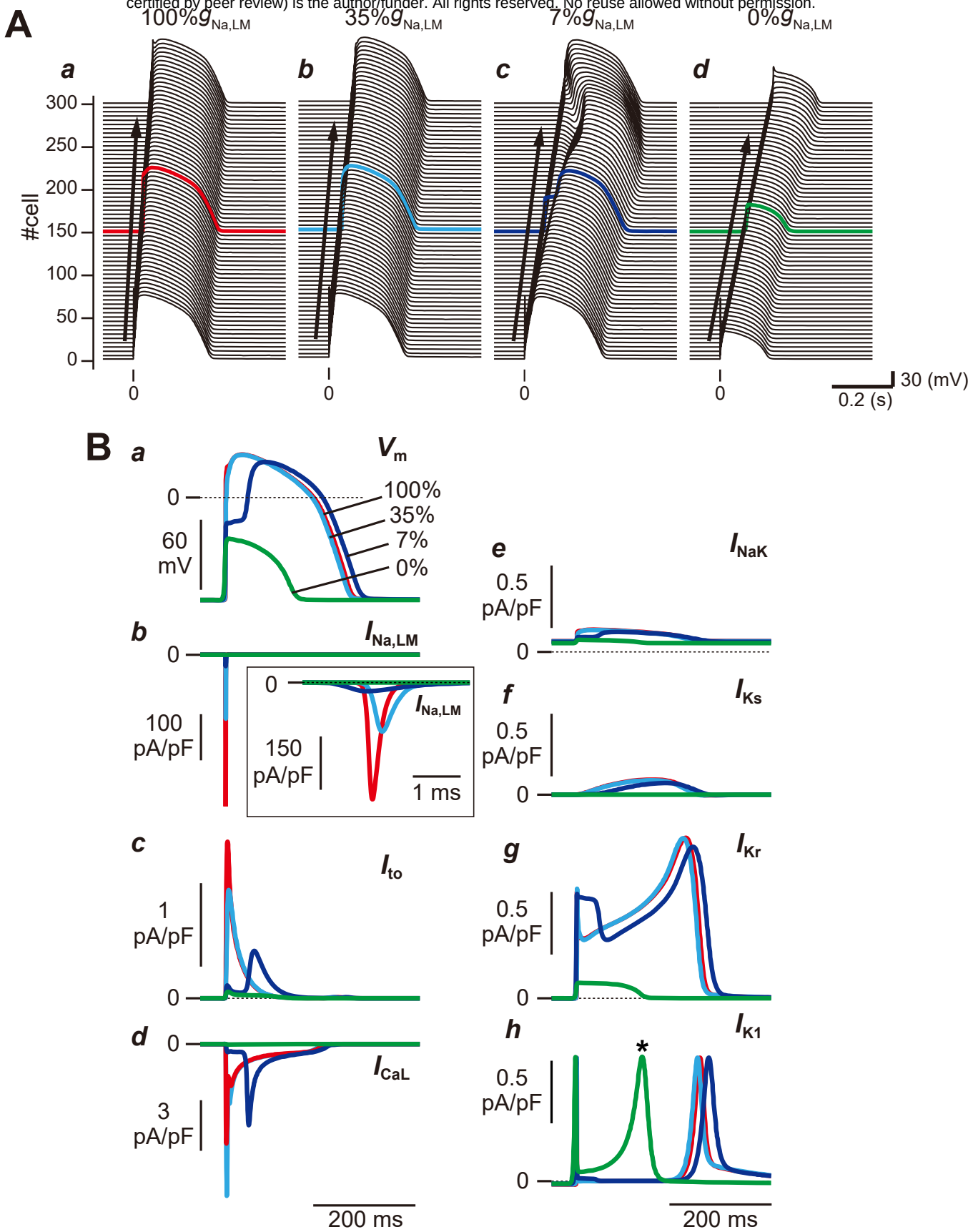

Figure 2

bioRxiv preprint doi: https://doi.org/10.1101/805986; this version posted October 16, 2019. The copyright holder for this preprint (which was not certified by peer review) is the author/funder. All rights reserved. No reuse allowed without permission.

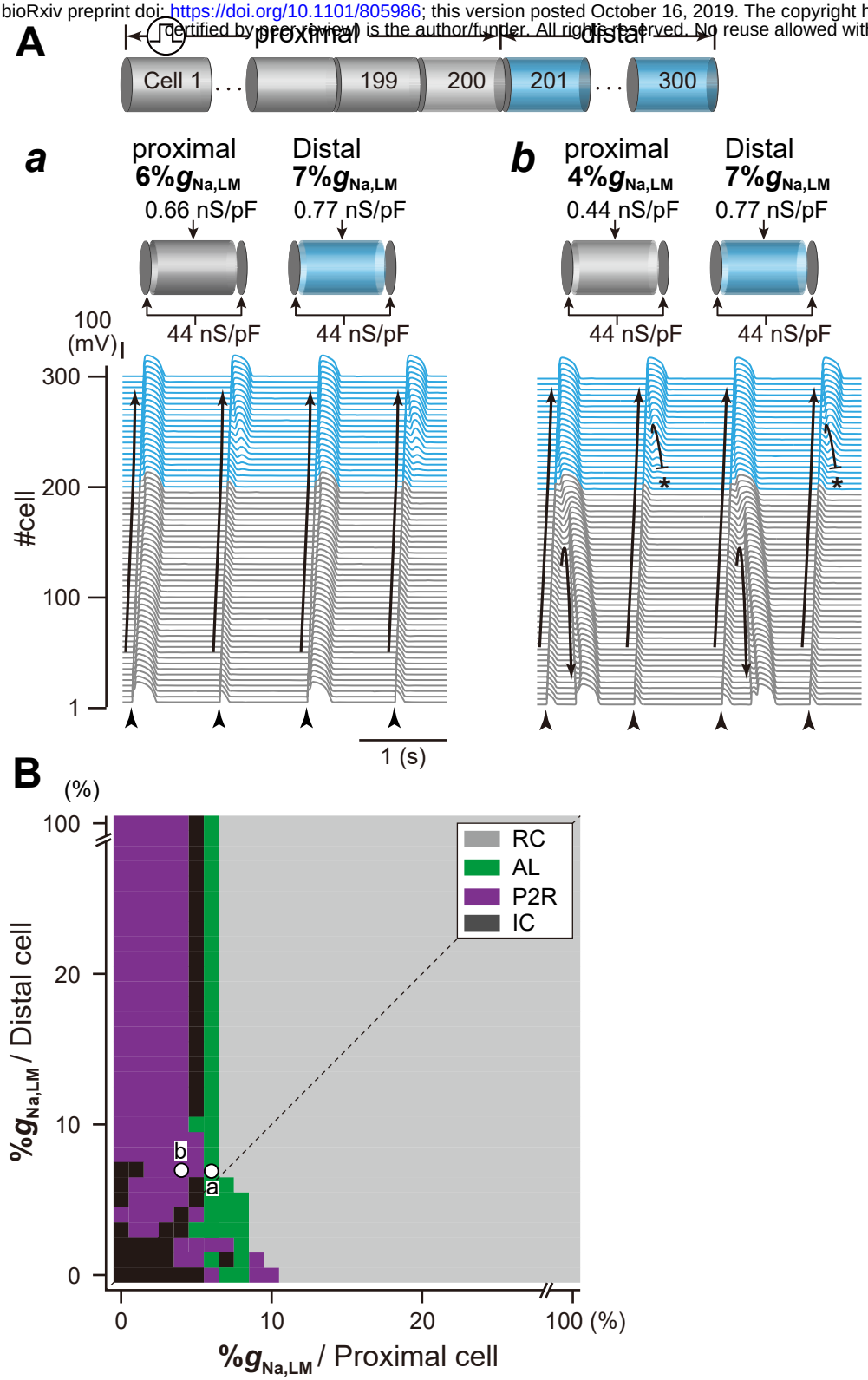

Figure 3

bioRxiv preprint doi: https://doi.org/10.1101/805986; this version posted October 16, 2019. The copyright holder for this preprint (which was not certified by peer review) is the author/funder. All rights reserved. No reuse allowed without permission.

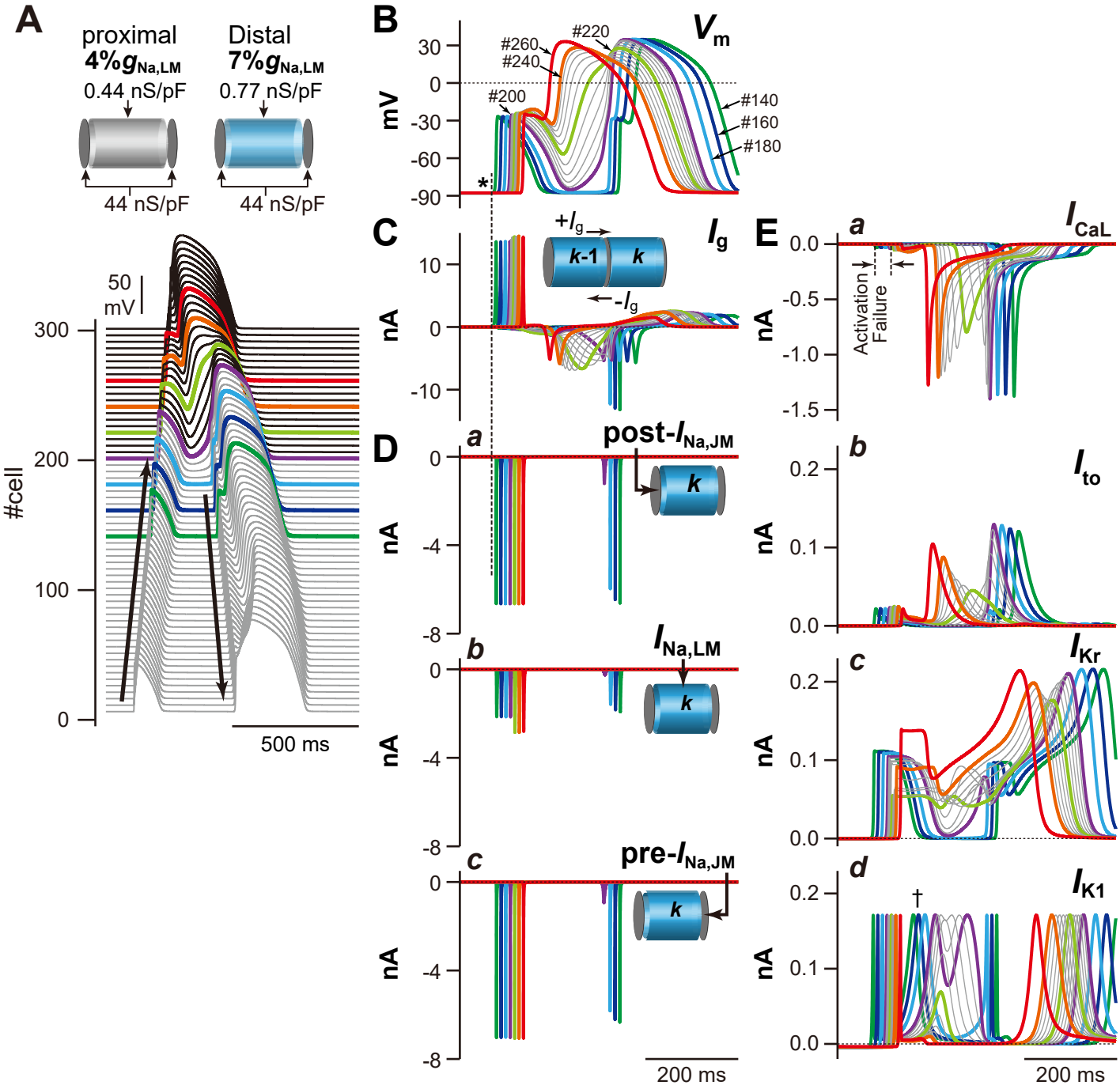

Figure 4

bioRxiv preprint doi: https://doi.org/10.1101/805986; this version posted October 16, 2019. The copyright holder for this preprint (which was not certified by peer review) is the author/funder. All rights reserved. No reuse allowed without permission.

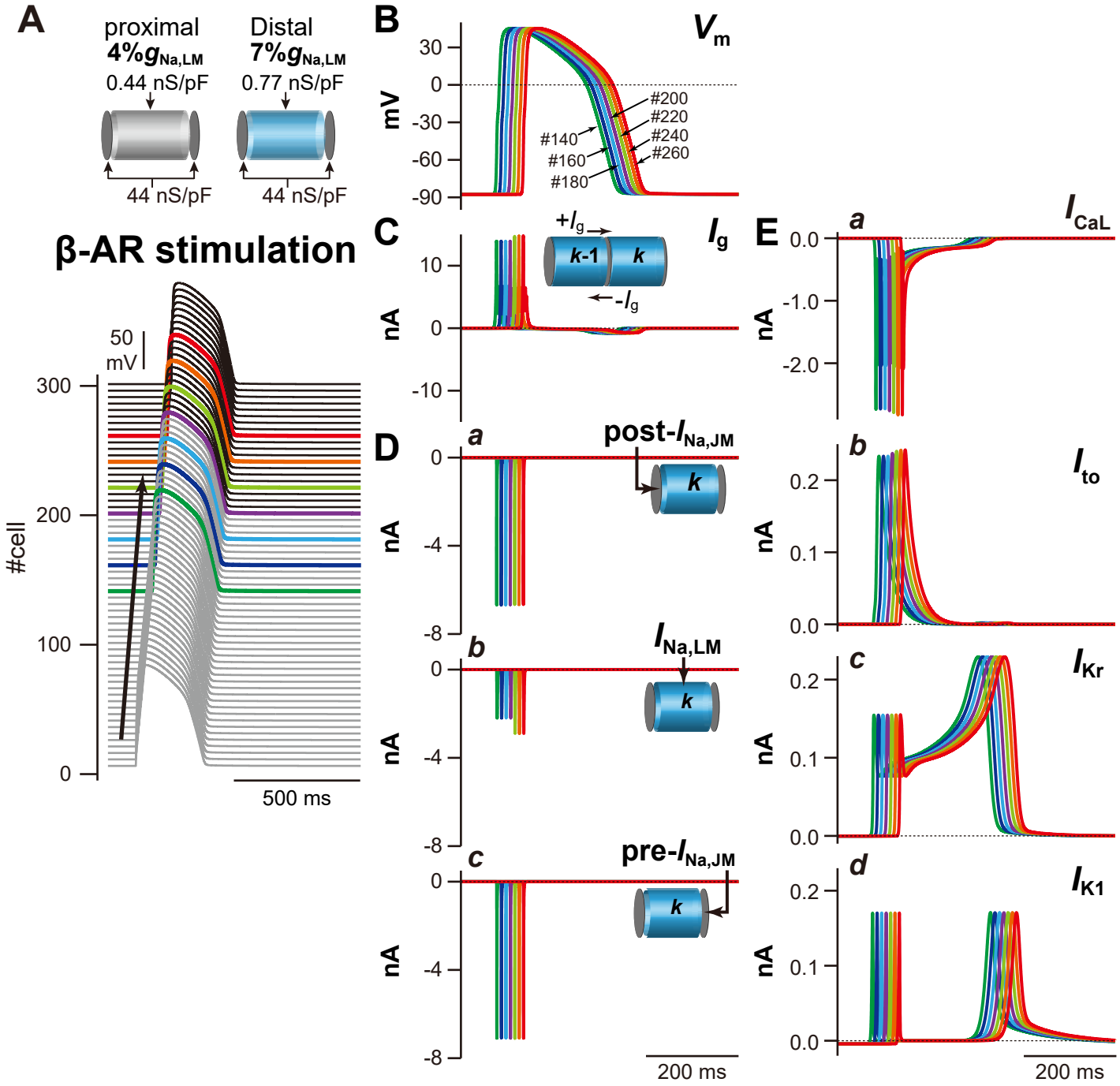

Figure 5

bioRxiv preprint doi: https://doi.org/10.1101/805986; this version posted October 16, 2019. The copyright holder for this preprint (which was not certified by peer review) is the author/funder. All rights reserved. No reuse allowed without permission.

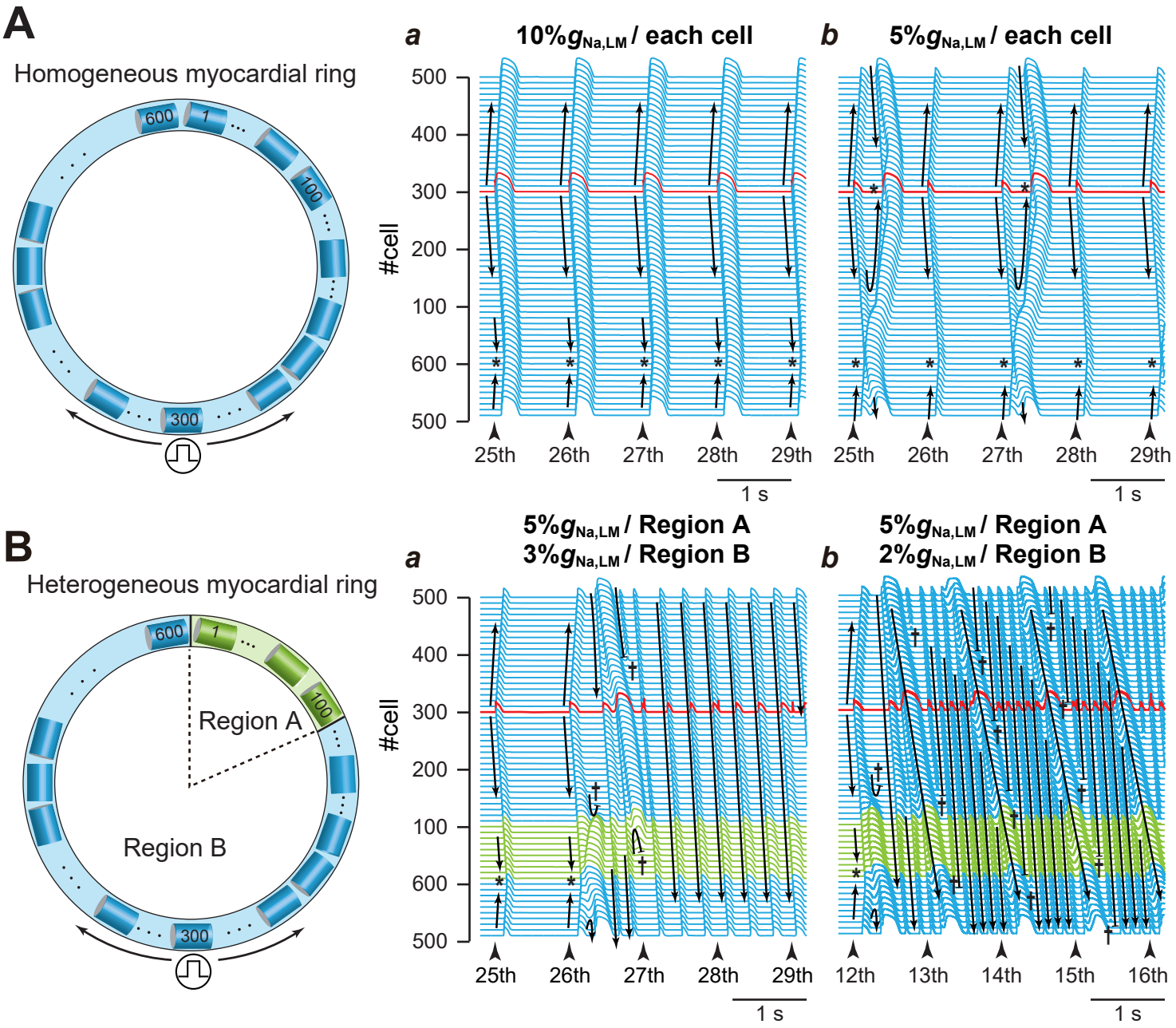

Figure 6

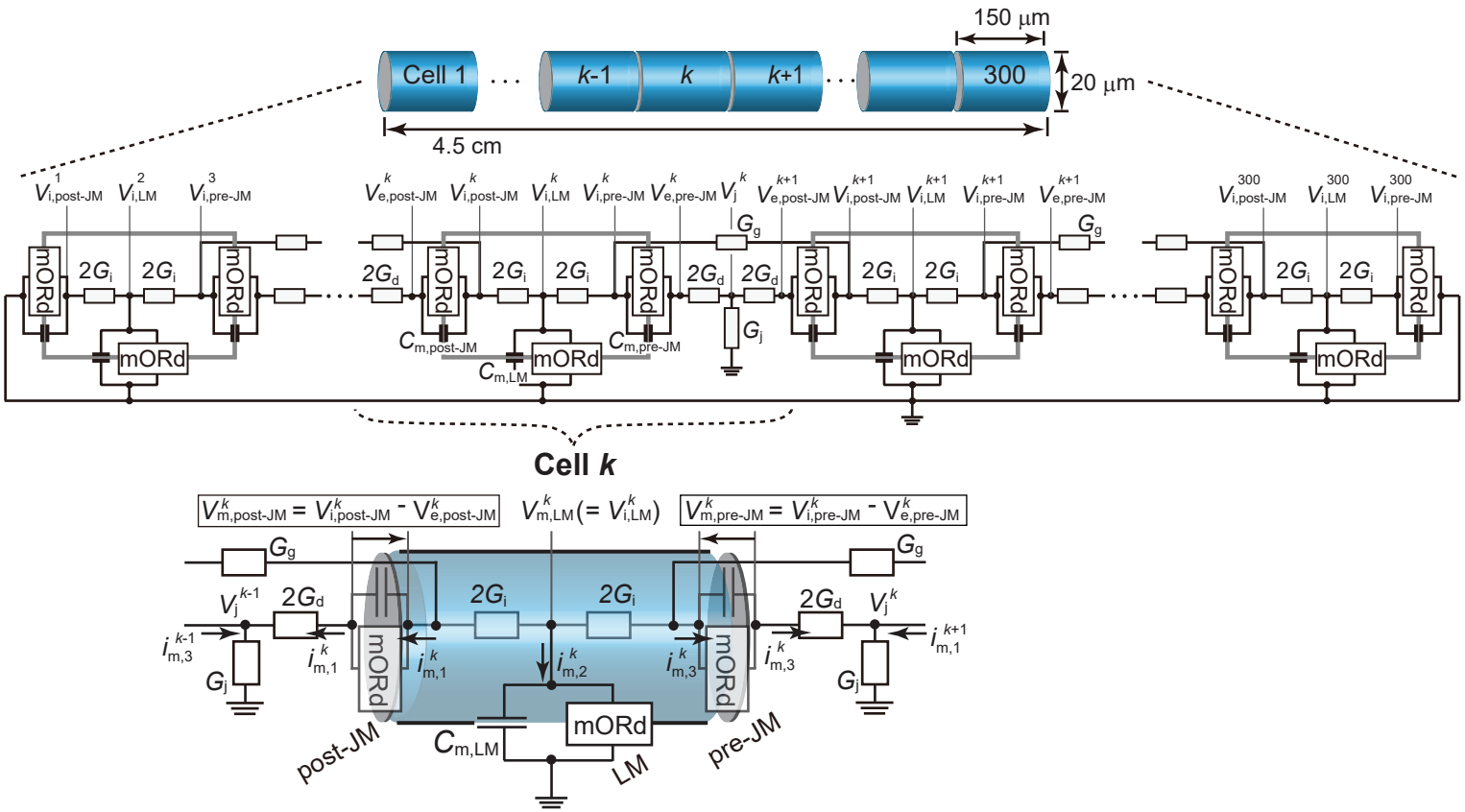

Figure S1

bioRxiv preprint doi: https://doi.org/10.1101/805986; this version posted October 16, 2019. The copyright holder for this preprint (which was not certified by peer review) is the author/funder. All rights reserved. No reuse allowed without permission.

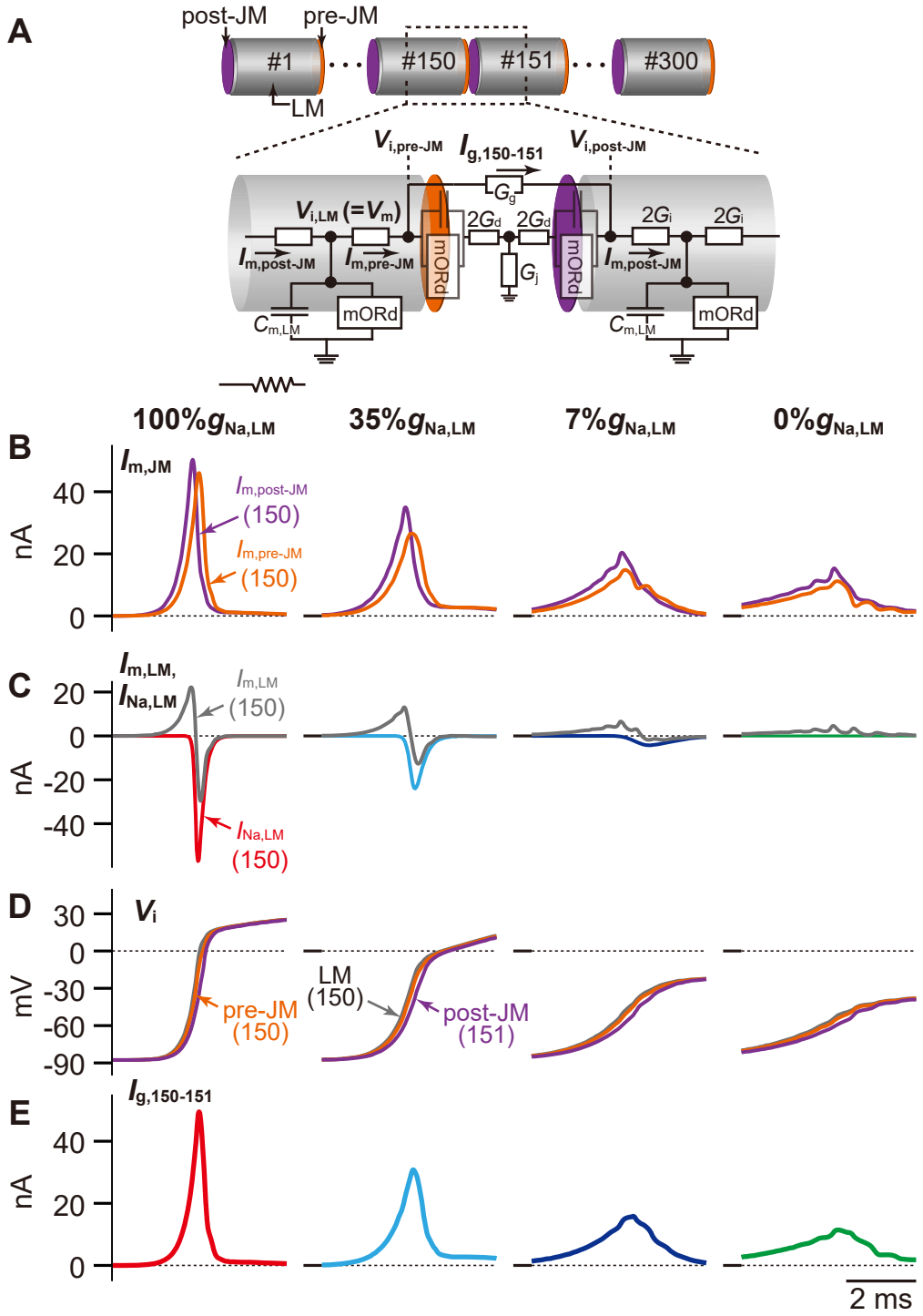

Figure S2

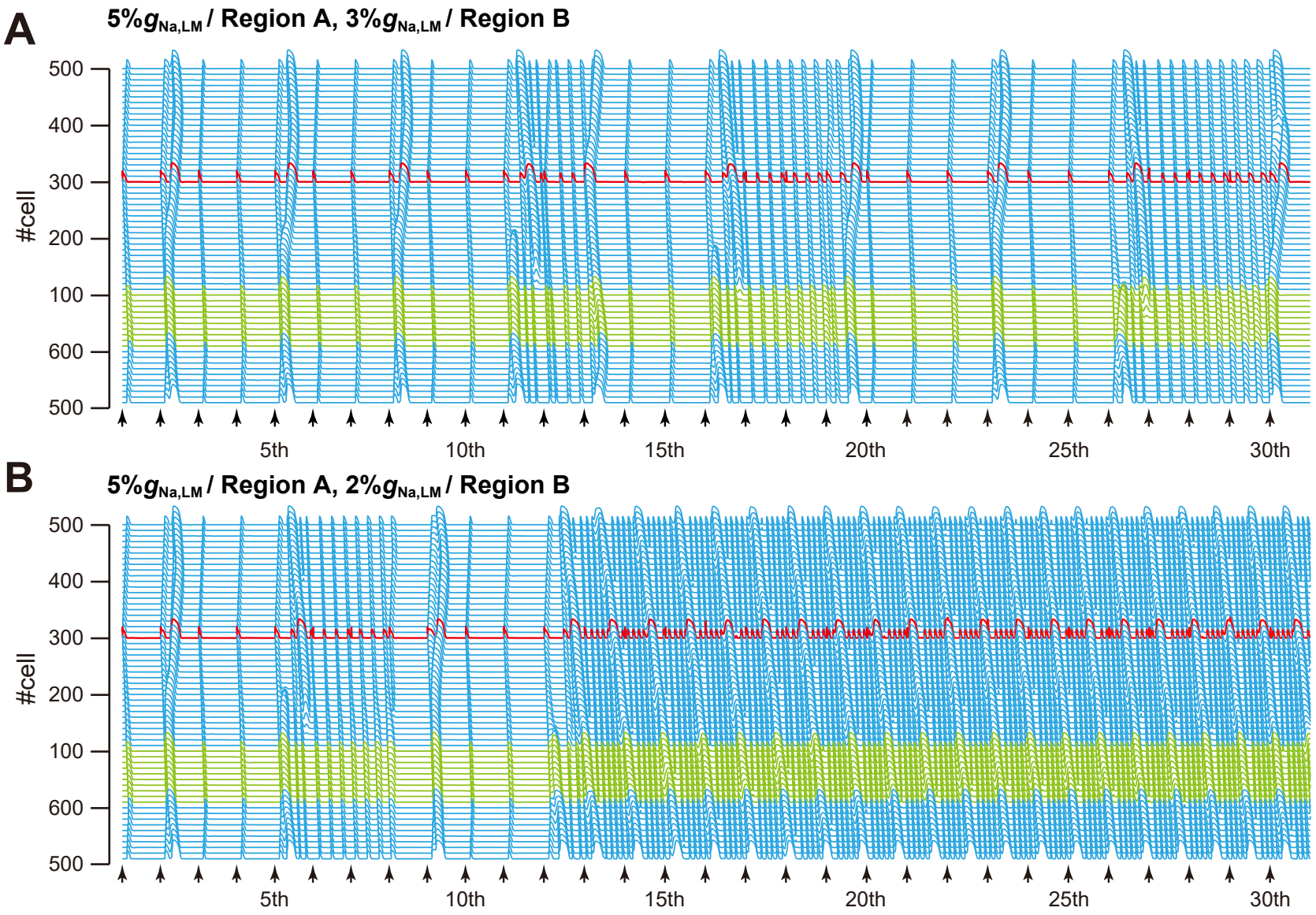
A
5%$g_{Na,LM}$ / Region A, 3%$g_{Na,LM}$ / Region B
#cell
500
400
300
200
100
600
500
5th
10th
15th
20th
25th
30th
B
5%$g_{Na,LM}$ / Region A, 2%$g_{Na,LM}$ / Region B
#cell
500
400
300
200
100
600
500
5th
10th
15th
20th
25th
30th

Figure S3